

INTERACTION BETWEEN Pd AND SiC: A STUDY FOR TRISO NUCLEAR FUEL

by

Goverdhan Reddy Gajjala

Bachelor of Science in Electrical Engineering
Osmania University College of Engineering, India
April 2003

A thesis submitted in partial fulfillment
of the requirements for the

Master of Science Degree in Engineering
Department of Electrical & Computer Engineering
Howard R. Hughes College of Engineering

Graduate College
University of Nevada, Las Vegas
May 2006

Thesis Approval Form
Provided by the Graduate College

ABSTRACT

Interaction between Pd and SiC: A Study for TRISO Nuclear Fuel

by

Goverdhan Reddy Gajjala

Dr. Rama Venkat, Examination Committee Chair
Professor & Chair of Electrical & Computer Engineering
University of Nevada, Las Vegas

and

Dr. Clemens Heske, Examination Committee Chair
Assoc. Professor, Dept. of Chemistry
University of Nevada, Las Vegas

The unique properties of SiC (wide band gap, high thermal conductivity, high electron mobility, and resistance to radiation effects) permits it to operate reliably at very high temperatures even in harsh environments and as coating layers in TRISO nuclear fuels. To optimize the SiC for use as a coating material in the nuclear reactor fuel design, it is important to elucidate the chemical bonding and interface formation of metal fission products (Pd, Ag, Cs, etc.) with SiC coating layers and to study the diffusion behavior of fission products into TRISO coating materials. It is known in the TRISO community that Pd is able to corrode the SiC layer. However, the detailed nature of this corrosion is still unknown.

The objective of this thesis is to study the influence of fission products (Pd) on the chemical and electronic properties of the SiC coating layer in TRISO nuclear fuel particles. For this purpose, three series of interfaces (Pd/SiC) were prepared and studied

using X-ray Photoelectron Spectroscopy (XPS) and Ultraviolet Photoelectron Spectroscopy (UPS).

The experimental approach comprises the preparation of Pd/SiC interfaces in-situ in our ultra-high vacuum system by electron-beam deposition of Pd onto suitable prepared SiC single crystal surfaces. In order to understand the impact of the SiC surface properties on the interface formation, a variety of surface preparation and modification schemes were employed. The results obtained give detailed information about the Pd/SiC interface formation. Thereby the study shows a diffusion at this interface, which is an important first step in understanding the corrosion of the SiC-layer in the TRISO particles.

TABLE OF CONTENTS

ABSTRACT.....	iii
LIST OF FIGURES	vii
ACKNOWLEDGMENTS	ix
CHAPTER 1 INTRODUCTION	1
1.1 TRISO fuel particle.....	1
1.2 Basis for the present study	4
CHAPTER 2 LITERATURE REVIEW	5
2.1 SiC surface studies.....	5
2.2 Mechanisms of Pd-SiC interaction	8
2.2.1 Behavior of Pd in UO ₂ kernels.....	9
2.2.2 Influence of kernel composition	11
2.2.3 Concentration dependence.....	12
2.2.4 Behavior in conjunction with rare earth fission products.....	12
2.2.5 Influence of the SiC properties	13
CHAPTER 3 EXPERIMENTAL.....	15
3.1 Measuring methods.....	15
3.1.1 X-ray Photoelectron Spectroscopy (XPS)	17
3.1.2 Ultraviolet Photoelectron Spectroscopy (UPS)	18
3.1.3 Auger-Electron Spectroscopy (AES).....	19
3.2 Instrumentation	19
3.2.1 Ultra High Vacuum (UHV)	20
3.2.2 Sample Handling.....	21
3.2.3 Sample treatment	22
3.2.4 X-Ray Source.....	23
3.2.5 Concentric Hemispherical Analyzer (CHA).....	25
3.2.6 Electron detector	26
3.2.7 E-beam metal evaporator	26
CHAPTER 4 RESULTS AND DISCUSSIONS.....	28
4.1 Experimental series 1	29
4.2 Experimental series 2.....	32
4.3 Experimental series 3	47
4.4 Discussions	58

4.4.1	Sample state after the sputtering cycles	60
4.4.2	After the Pd deposition steps	61
CHAPTER 5 CONCLUSIONS AND FUTURE WORK		65
5.1	Conclusions.....	65
5.2	Future Work.....	67
BIBLIOGRAPHY		65
VITA		71

LIST OF FIGURES

Figure 1-1 TRISO fuel concept showing the fuel particles, fuel compacts, and fuel assembly blocks [6].	3
Figure 2-1 Low energy electron diffraction (LEED) pattern recorded for selected surface structures at 95 eV electron energy: the pure (3 x 3), (3 x 3) with already dominating (2 x 2) _C , pure (2 x 2) _C . (Black indicates high electron intensities) [16].	6
Figure 2-2 Schematic representation of the corrosion mechanism of the TRISO SiC layer by the fission product palladium [7].	8
Figure 2-3 Pd penetration rate into SiC based on international data [25].	11
Figure 2-4 Pd penetration rate into SiC as a function of SiC coating rate [8].	14
Figure 3-1 Schematic diagram of core-level ionization (photoemission) in a semiconductor. The two competing secondary processes for filling the core hole (Auger-electron and X-ray emission) are also sketched. <i>Solid arrows</i> correspond to electrons, <i>dashed arrows</i> to photons [29].	16
Figure 3-2 SiC survey spectrum.	18
Figure 3-3 Picture of the ESCA in the Chemistry Dept., UNLV.	20
Figure 3-4 Concentric Hemispherical Analyzer (CHA)	26
Figure 3-5 The e-beam metal evaporator and its various parts	27
Figure 4-1 Survey spectrum of the as-introduced SiC sample of series 1.	29
Figure 4-2 Peak fit analysis of the C 1s peaks before and after Pd deposition on 6H-SiC(0001). The C 1s Species shown are (a) a bulk species, (b) a surface species before Pd deposition and (a) a bulk species, (b) an interface species, and (c) a reacted species after Pd deposition.	31
Figure 4-3 Peak fit analysis of Si 2p. Before Pd deposition (a) a bulk species and (b) a surface species are found; after Pd deposition, (a) a surface species and (b) an interface species are shown.	32
Figure 4-4 Sequence of survey spectra from series 2.	33
Figure 4-5 C 1s XPS spectra from series 2.	34
Figure 4-6 Peak fit analysis of the C 1s spectra.	35
Figure 4-7 Area percentages of all three C 1s species of the second series.	36
Figure 4-8 Si 2p XPS spectra, second series.	37
Figure 4-9 Peak fit analysis of the Si 2p spectra, second series.	38
Figure 4-10 Percent area plot of the Si 2p species.	39
Figure 4-11 Pd 3d _{3/2} spectra as a function of deposition step.	40
Figure 4-12 Comparison of Pd 3d _{3/2} peaks for the thickest and thinnest Pd film.	40
Figure 4-13 Relative binding energy change in the peak positions of C 1s, Si 2p, and Pd 3d _{3/2} .	42

Figure 4-14 Sequence of UPS survey spectra for the second series, taken with a bias voltage of 15 V and not taking the work function of the electron analyzer into account.....	43
Figure 4-15 Secondary electron cut-off spectra of the second sample series.....	44
Figure 4-16 Au reference spectrum.....	44
Figure 4-17 Upper valence band spectra of the second sample series.....	45
Figure 4-18 Position of the valence band maximum/Fermi edge for the second sample series.....	46
Figure 4-19 Work Function plot of the sample.....	46
Figure 4-20 Sequence of XPS survey spectra of series 3.....	47
Figure 4-21 Sequence of C 1s XPS spectra.....	48
Figure 4-22 Peak fit analysis of C 1s spectra.....	49
Figure 4-23 Area percentages of all three species of C1s, third series.....	50
Figure 4-24 Si 2p XPS spectra, third series.....	51
Figure 4-25 Peak fit analysis of the Si 2p spectra. Before Pd deposition, (a) bulk, (b) surface species; and after Pd deposition, (a) surface, (c) interface species are seen. An additional species (d) can also be seen after the last deposition step.....	52
Figure 4-26 Percent area plot of Si 2p, third series.....	53
Figure 4-27 Pd 3d _{3/2} spectra as a function of Pd deposition.....	53
Figure 4-28 Relative change in the peak positions of C 1s, Si 2p, and Pd 3d _{3/2}	54
Figure 4-29 Sequence of UPS survey spectra for the third series, taken with a bias voltage of 15 V and not taking the work function of the electron analyzer into account.....	55
Figure 4-30 Secondary electron cut-off spectra of the third sample series.....	56
Figure 4-31 Upper valence band spectra of the third series.....	56
Figure 4-32 Position of the valence band maximum/Fermi edge for the third sample series.....	57
Figure 4-33 Work Function plot of the sample at each step.....	58
Figure 4-34 Formation of a Schottky barrier (for the case of metal with a larger work function than the semiconductor, as in the present case).....	59
Figure 4-35 Band scheme of the sample after sputter-cleaning.....	61
Figure 4-36 Band scheme of the Pd-SiC interface after the 1 st Pd deposition.....	62
Figure 4-37 Band scheme of the Pd-SiC interface after further Pd deposition.....	64

ACKNOWLEDGMENTS

I would like to dedicate this thesis to my parents, brother, Sandhya and friends whose love, support and understanding have always motivated me to strive for excellence.

I would like to sincerely and wholeheartedly thank Dr. Clemens Heske for his guidance and kindness throughout this work. His patience as an advisor, boundless energy while teaching, promptness while reviewing all my writing, and passion for research are to be commended and worth emulating. I am indebted to him for cajoling me into doing experiments and I owe most of this work to him.

I am very grateful to my advisor, Dr. Rama Venkat, Chair of Electrical and Computer Engineering, for his extreme support and the valuable guidance he provided during this project.

A special thanks and appreciation to our group, Lothar Weinhardt, Timo Hofmann, Varun Marepally, Marcus Baer, Moni Blum, Jared White, and Kyle George who helped me a lot throughout this work.

CHAPTER 1

INTRODUCTION

Two distinct nuclear processes involving the nuclei of atoms for energy production are: fission—the splitting of a nucleus—and fusion—the joining together of two nuclei. For any given mass or volume of fuel, nuclear processes generate more energy than can be produced through any other fuel-based approach. In the case of nuclear fission, in which the nucleus of an atom splits into two or more smaller nuclei (fission products), heat and then electricity is generated from the energy released.

Fission power currently provides about 17 percent of the world's electric power. However, several problems like disposal of radioactive waste, concern about nuclear weapons proliferation, concern about safe operation of plants, and failure mechanisms of the nuclear fuel question fission's potential as an acceptable power source today and in the future [1].

1.1 TRISO fuel particle

The TRISO-coated fuel particles consist of a microspherical kernel of a radius ~ 175 μm made of oxide or oxycarbide fuel and a coating made of porous pyrolytic carbon (PyC), an inner layer made of dense PyC (IPyC), a silicon carbide layer (SiC), and an outer layer made of dense PyC (OPyC) as shown in Figure 1-1. The function of these coating layers is to retain fission products within the particle. The porous PyC coating

layer, called the buffer layer, attenuates fission recoils and provides void volume for gaseous fission products and carbon monoxide. The IPyC coating layer acts as containment to gases during irradiation and protects the fuel kernel from the reaction with the coating gases during the SiC coating process. The SiC coating layer provides mechanical strength for the particle and acts as a barrier to the diffusion of metallic fission products, which diffuse easily through the IPyC layer. Finally, the OPyC coating layer protects the SiC coating layer mechanically [2].

The SiC layer provides the primary barrier for both radioactive elements in the kernel and gaseous and metallic fission products. Corrosion or thinning of the SiC lead to a fracture of the coating layers or provide a localized path for the escape of fission products by diffusion from the fuel particle. These radionuclides might reach the cooling circuit, and ultimately result in maintenance and safety problems. So, the performance of these fuel particles is a key component in system containment and depends heavily on the properties and performance of the silicon carbide layer [3-5].

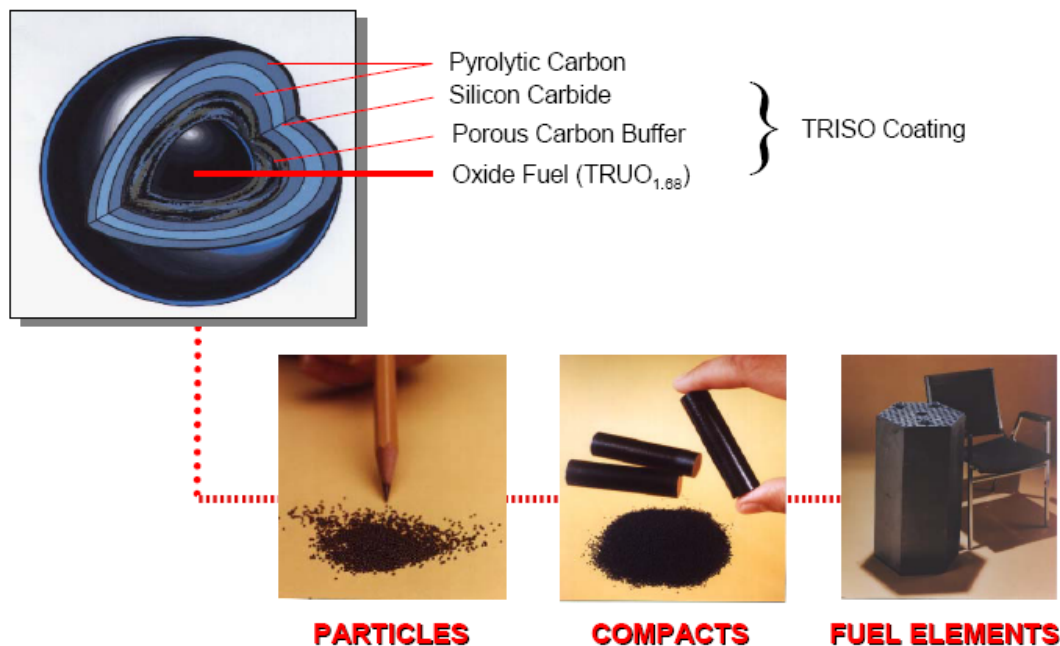


Figure 1-1 TRISO fuel concept showing the fuel particles, fuel compacts, and fuel assembly blocks [6].

Chemical interaction of the SiC coating layer with fission products is one of the possible performance limitations of the TRISO-coated fuel particles. Corrosion of the SiC layers by the fission product palladium (Pd) has been observed in irradiated TRISO-coated fuel particles [7-9]. The Pd-SiC interaction can degrade the capability of retaining fission products within the particle. Moreover, once the SiC coating is breached by the release of palladium, other hazardous fission products, such as Cs, Ag, and Sr can be released from the fuel particles. The degradation of the SiC layer is considered to be one of the main factors leading to coating failure. Besides the irradiation experiments, post-irradiation heating tests of the coated particles and out-of-reactor experiments on the Pd-SiC interactions have been reported. But the mechanism of the corrosion of the SiC layer

by palladium has not been understood clearly and data on the Pd-SiC interaction in UO₂ fuel particles was limited [10].

1.2 Basis for the present study

The goal of this project is to elucidate the chemical bonding and the interface formation of metal fission products (palladium) with the coating materials (SiC) so that this helps in prevention of the release of fission products out of nuclear fuels.

Surface- and interface-sensitive spectroscopic methods like X-ray Photoelectron Spectroscopy (XPS) and Ultraviolet Photoelectron Spectroscopy (UPS) were used to elucidate the chemical nature of the interface between Pd and SiC [11]. This study adds a new point of view to the existing discussion on the SiC coating layer in TRISO nuclear fuels, because it gives a direct insight into the electronic structure and hence into the nature of the chemical bonding at the interface. It sheds light on the chemical stability of TRISO particles with respect to diffusion of Pd through the SiC coating material layer and the corresponding interface. Based on a detailed analysis of the interface properties, surface and interface modification treatments for an enhanced stability of TRISO-fuel particles can be proposed in the future.

A literature review of the relevant work related to SiC surface study and corrosion of SiC by Pd in nuclear fuels will be presented in Chapter 2. The experimental setup and procedures for measuring, cleaning of the sample (SiC) by sputtering and annealing, and deposition of Pd on SiC will be described in Chapter 3. Results and discussions will be presented in Chapter 4. A summary of this thesis and recommendations for future experiments are given in Chapter 5.

CHAPTER 2

LITERATURE REVIEW

The properties of SiC, such as wide band gap, high thermal conductivity, high electron mobility, and resistance to radiation effects make it a desirable semiconductor for high temperature operations, high power microelectronics, as well as for coating layers in TRISO nuclear fuels. These unique properties permit SiC to operate reliably at very high temperatures even in harsh environments. A detailed literature study about the SiC surfaces and the chemical interactions of fission products with TRISO particles is given in this chapter. To compare with the literature results, note that the SiC single crystal surface that was used for this work was 6H-SiC(0001).

2.1 SiC surface studies

Many polytypes of SiC (e.g., 3C-, 4H- and 6H-SiC) exist, differing only in the stacking sequence of the hexagonal bilayers of alternating silicon and carbon atoms [12]. The clean surfaces of 3C-, 4H- and 6H-SiC are strongly reconstructed and have different structures depending on how the surface was prepared. For example, in the case of 6H-SiC(0001)-Si (Si-terminated), the surface can show three different types of reconstructions: (i) 3×3 , (ii) $\sqrt{3}\times\sqrt{3}$ and (iii) 6×6 [13]. Annealing the Si-predeposited surface at 850 °C in ultra-high vacuum (UHV) leads to a 3×3 surface, which is changed

to a $\sqrt{3}\times\sqrt{3}$ reconstruction by further annealing at 950 °C. Further heating above 1000°C forms a $6\sqrt{3}\times6\sqrt{3}$ structure. When the (0001) surface is flashed to 1150 °C, it is graphitized and takes a 6×6 structure. It is believed that the $6\sqrt{3}\times6\sqrt{3}$ surface is a mixture of the $\sqrt{3}\times\sqrt{3}$ and 6×6 domains [14]. The 6H-SiC(0001)- $\sqrt{3}\times\sqrt{3}$ surface consists of Si adatoms of 1/3 of a monolayer on top of the Si-C bilayer. It was also found that the SiC(0001)- 3×3 surface comprises the silicon adatoms supported by trimers on the Si adlayer which is located on the first Si-C bilayer. This indicates that the oxidized surface structure is not homogeneous and SiO₂-like domains accompanied by some SiC_xO_y-silicate with a C-O bond are formed [15].

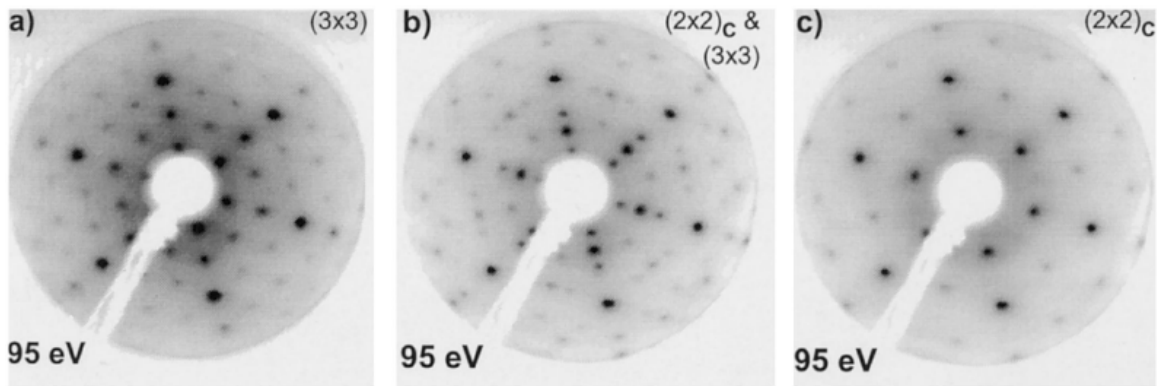


Figure 2-1 Low energy electron diffraction (LEED) pattern recorded for selected surface structures at 95 eV electron energy: the pure (3 x 3), (3 x 3) with already dominating (2 x 2)_C, pure (2 x 2)_C. (Black indicates high electron intensities) [16].

Bernhardt et al. investigated the initial oxidation of the 6H-SiC(0001)- $\sqrt{3}\times\sqrt{3}$ surface was analyzed in-situ by medium energy ion scattering and synchrotron-based photoelectron spectroscopy, to determine the absolute quantity of adsorbed oxygen and

measure the fraction of the different oxidation states of Si as well as the surface band structure [16]. Their Si 2p and C 1s core level analysis, taking the absolute amount of adsorbed oxygen into account, indicates that all adatoms are easily oxidized at RT and a small amount of oxygen (10–15%) is inserted into the Si–C bond. The oxidation at 500 °C proceeds inhomogeneously, not in a layer-by-layer fashion, and leads to formation of SiO₂-like domains accompanied by some SiC_xO_y-silicate with a C–O bond [12].

However, for the reverse crystal orientation, namely (000 $\bar{1}$), starting from ex-situ prepared (1×1)-ordered surfaces, heating of the sample in ultra-high vacuum leads to (3×3), (2×2)_C (carbon terminated), and (1×1)_{graphitic} phases with increasing temperature (Figure 2-1). Starting either from ex-situ prepared (1×1)/(√3×√3)R30° or in-situ prepared (2×2)_{Si} (silicon terminated) surface structures, a (3×3) phase is observed when heating the surface to about 1050°C, which is accompanied by a silicon depletion of the surface. Careful annealing of this structure at 1075°C leads to the development of a slightly less Si-depleted (2×2)_C phase which, with the (3×3) phase gradually vanishing, finally dominating the surface structure. Using higher annealing temperatures ($T \geq 1150^\circ\text{C}$) leads to a strong carbon enrichment of the surface, accompanied by the transition of the (2×2)_C pattern to (1×1) symmetry with significant background intensity indicating an increasing disorder. The only stable silicon-rich surface phase is the (2×2)_{Si} phase, which can either be prepared through additional Si deposition while heating the sample at 1150°C or by heating a surface covered with a Si film of thickness $d_{\text{Si}} \geq 20 \text{ \AA}$ [17].

All the details about the various surface structures of SiC were presented because it gives a first indication of chemical reactivity of the surface, which will be important for Pd as well.

2.2 Mechanisms of Pd-SiC interaction

Silicon Carbide is the primary barrier to metallic fission product release from TRISO coated-particle fuels. Consequently, any degradation of the coating should be minimized.

The mechanism of the corrosion of the SiC layers by the fission product palladium can be described as a series of sequential steps: (1) birth of palladium by fission in the fuel kernel, (2) release of palladium from the fuel kernel, (3) transport of palladium to the SiC layer through the PyC layers, and (4) reaction of palladium with the SiC layer. These steps are shown schematically in Figure 2-2. Of these steps, the slowest one limits the Pd-SiC reaction rate [7].

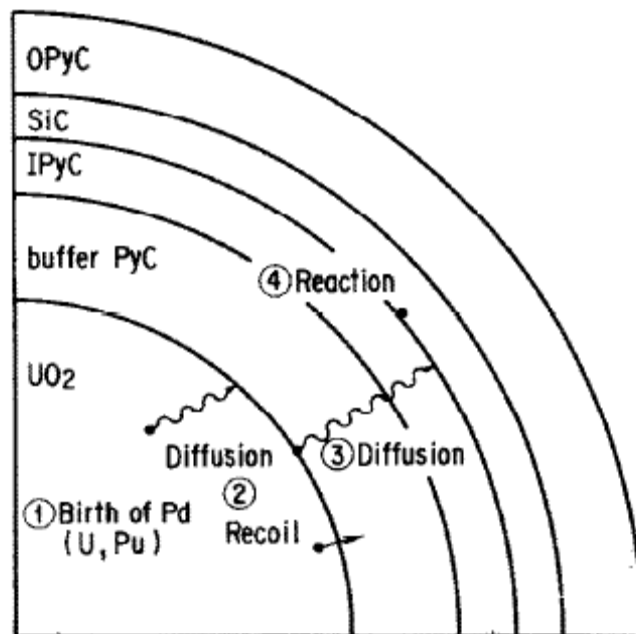


Figure 2-2 Schematic representation of the corrosion mechanism of the TRISO SiC layer by the fission product palladium [7].

Tiegs et al. [8] report that the rate of SiC corrosion by palladium was mainly dependent on the irradiation temperature and found that other factors, such as kernel composition, palladium concentration, the presence of other fission products, and the properties of the SiC layer, were secondary.

In the case of the UO₂ coated particles, palladium was observed in the fuel kernels, which indicates that the birth rate of palladium (step (1)) does not limit the Pd-SiC reaction rate. The birth rate of palladium depends on the fission rate of the heavy metal atoms in the TRISO particle. In the case of the low-enriched fuel, the contribution of ²³⁹Pu fission increases with burnup, which results in an increase in palladium yield since the fission yield of palladium from ²³⁹Pu is much larger than that from ²³⁵U [18].

Step (3) would also not limit the reaction rate, since the diffusion of palladium in the PyC is fast [19] and in fact no palladium was observed in the PyC layers. Among the first three steps, it is thus the release of palladium from the kernel, that controls the Pd-SiC reaction. Therefore the factors influencing the reaction are the composition of the fuel kernel, the palladium birth rate, irradiation temperature, and time. Furthermore, and that is the primary focus of this present study, step (4) will play a central role, and thus is important to gain insight into the actual reaction mechanism between Pd and SiC.

2.2.1 Behavior of Pd in UO₂ kernels

In intact coated UO₂ particles, Pd is usually found in metallic inclusions, together with, e.g., molybdenum, technetium, ruthenium, and rhodium [20-23]. It was also found that the atomic ratios of palladium to ruthenium and palladium to rhodium in the inclusions were smaller than those in the expected fission yields. This result indicates that palladium is released more easily from the UO₂ kernel than rhodium and ruthenium. The

higher release fraction of palladium from the kernel can be attributed to the high vapor pressure of palladium in the inclusion [24].

The fission product palladium is known to attack SiC at localized reaction sites. In high burnup low-enriched Uranium (LEU) fuels, 25 to 50 times more Pd is produced than in either high-burnup, high-enriched Uranium (HEU) fuels or LEU low-burnup fuels because of the large fraction of fissions from Pu expected at high burnup. As a result, the potential for Pd attacking of SiC will be higher in LEU high burnup fuels. A review of the international database, performed in [25], shows no strong dependence on burnup or the composition of the kernel (discussed below), although theoretically this could be important [25]. The penetration rate of Pd into SiC is found to have an Arrhenius relationship with temperature [8] (Figure 2-3), that is,

$$P = A \cdot \exp(-Q/RT),$$

where

P = rate of penetration of SiC, $\mu\text{m/h}$

A = preexponential constant, $\mu\text{m/h}$

Q = activation energy, J/mol

R = gas constant, 8.314 J/ (mol·K)

T = temperature, K.

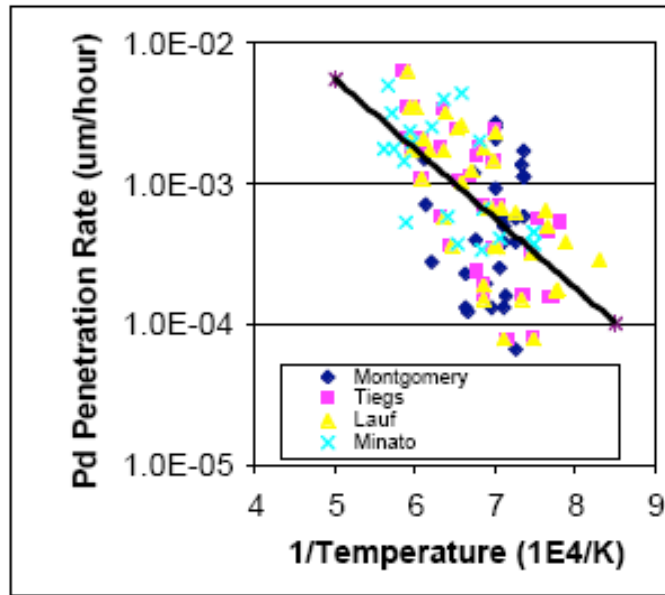


Figure 2-3 Pd penetration rate into SiC based on international data [25].

2.2.2 Influence of kernel composition

Kernel composition plays no direct role in the Pd-SiC interaction, but does affect the release of palladium and other fission products from the kernel. Palladium is released from the kernel and resides at the inner surface of the SiC coating. Although some palladium can be held in the kernel, most of the palladium in a particle is released from the kernel regardless of the composition and is free to migrate to the SiC coating.

Release of high-yield rare earth fission products like neodymium, cerium, praseodymium, and lanthanum from the kernel and their migration down the temperature gradient has been commonly observed with fuel kernels. The accumulation of these rare earth metals at the SiC coating coincides exactly with the palladium accumulation. Similar observations have been made with high-enriched dense UC_2 , except that the release of rare earth metals from the kernel was large enough that they not only were present in the palladium accumulations, but also were found in the surrounding area

adjacent to the SiC coating. Thus, although the kernel composition has little effect on the release of palladium, it does affect the release of the rare earth fission products [8].

2.2.3 Concentration dependence

The amount of palladium in a coated particle is a function of

1. heavy-metal burnup and palladium fission yield
2. kernel density
3. kernel volume

The fission yield of palladium isotopes varies considerably with the fissile species and is the largest single factor affecting the amount of palladium per particle. Thus, in particles with a high percentage of plutonium isotopes (LEU and plutonium fuels) instead of by ^{235}U or ^{233}U , the palladium generation rate per particle will be higher for comparable heavy-metal burnups. The concern over Pd-SiC interactions is greatest for coated-particle fuels having low enrichments of ^{235}U . Also, no threshold amount of palladium per particle is necessary before penetration occurs [8].

The palladium accumulates in distinct “nodules”, so that even with low amounts of palladium per particle, the concentration is high enough in localized areas to cause corrosion. Thereby the amount of Pd per particle only affects the number of nodules formed at the SiC coating [8].

2.2.4 Behavior in conjunction with rare earth fission products

As mentioned previously, the rare earth and palladium accumulations coincide with each other at the inner surface of the SiC coating for particles with fuel kernels. Also they are associated with each other during the penetration of the SiC coating.

The different sets of data observed are

1. rare earth and palladium penetration rates at temperatures $\geq 1300^\circ\text{C}$ [26]

2. rare earth with no palladium penetration at temperatures $\geq 1300^{\circ}\text{C}$ [27]
3. palladium with no rare earth penetration at temperatures $\leq 1400^{\circ}\text{C}$ ([8], see Figure 2-4)

These data suggest that at temperatures below 1400°C , palladium penetrates the SiC at rates faster than rare earths, but that at temperatures above 1400°C , the reverse is true. Because the average temperatures in a nuclear reactor are designed to be much less than 1400°C , palladium is the more important species for further study.

2.2.5 Influence of the SiC properties

The microstructure of the SiC layer affects the rate of palladium penetration, but the exact correlation between microstructural features and penetration rate is still unknown. Furthermore, it can be expected that the various surface reconstructions of SiC (discussed above) will have a significant impact on the Pd/SiC interface formation and the Pd penetration. Because the results of forming Pd/SiC interfaces with various SiC surface structures are encouraging for limiting palladium penetration, efforts are in progress to carefully examine SiC microstructures and their ability to suppress the corrosion caused by palladium [8]. Within our project and based on the results presented in this thesis, surface modification schemes to limit the chemical interaction between Pd and SiC will be tested.

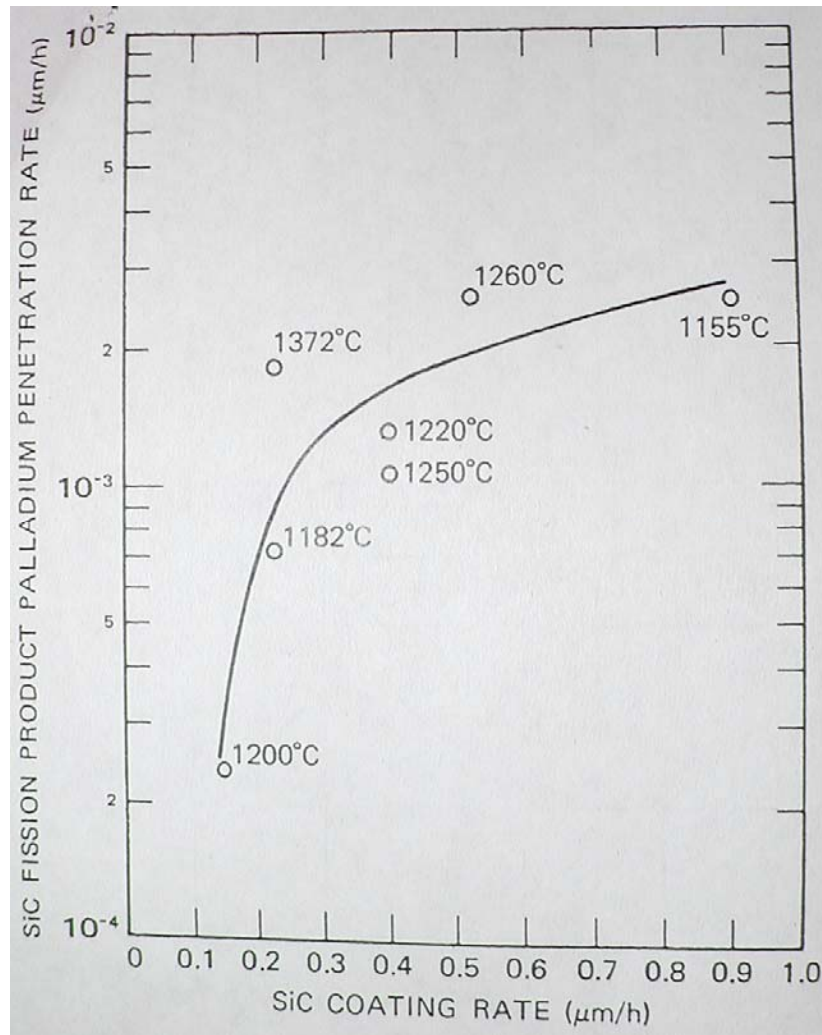


Figure 2-4 Pd penetration rate into SiC as a function of SiC coating rate [8].

CHAPTER 3

EXPERIMENTAL

Spectroscopic measurements are powerful tools in modern physics, and the interaction between light and matter is one of the primary experimental areas for probing the properties of solids. Especially important for studying electronic properties is light in the range of soft X-rays and the vacuum ultraviolet, which interacts with electrons in solids. Techniques such as photoelectron spectroscopy and X-ray emission spectroscopy are now standard tools for studying the electronic structure of materials [28]. In the present thesis, we use X-ray photoelectron spectroscopy (XPS) and UV photoelectron spectroscopy (UPS) to elucidate the electronic and chemical structure of the Pd/SiC interface.

3.1 Measuring methods

Applying soft X-ray spectroscopies to the study of surfaces and interfaces has been one of the prominent fields of Surface Science [29]. Photoelectron spectroscopy (PES), in particular, has become the standard method to study the chemical and element-specific properties of surfaces and interfaces [30]. As shown in Figure 3-1, PES involves the ionization of a valence or core level and the subsequent detection of the emitted electron w.r.t. its kinetic energy. The short inelastic mean free path of the emitted electrons makes PES a very surface-sensitive method [29].

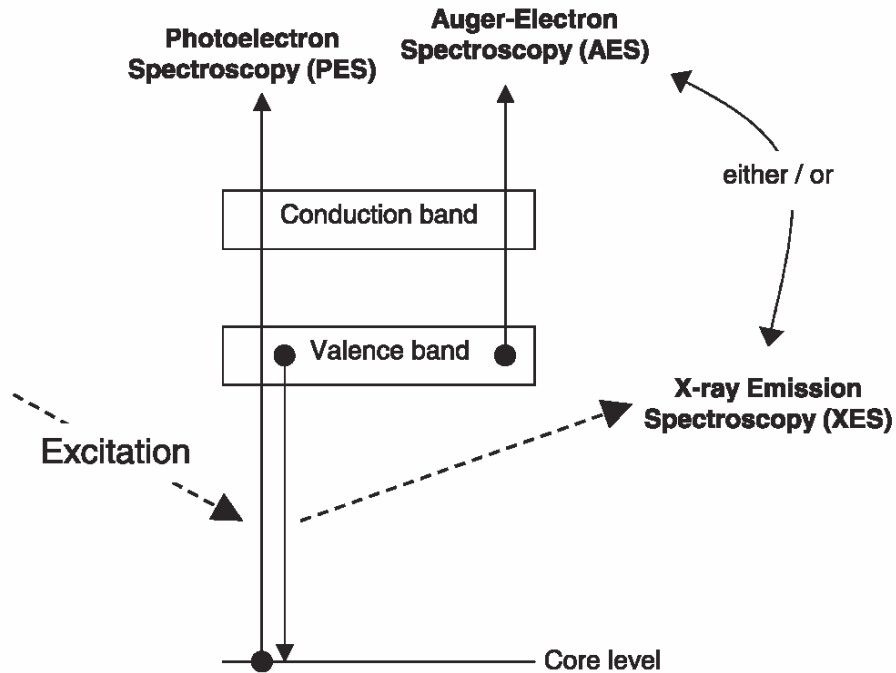


Figure 3-1 Schematic diagram of core-level ionization (photoemission) in a semiconductor. The two competing secondary processes for filling the core hole (Auger-electron and X-ray emission) are also sketched. *Solid arrows* correspond to electrons, *dashed arrows* to photons [29].

A hole in an ionized core level is filled by a weak bound electron. As shown in the Figure 3-1, there are two ways to conserve energy in the process of filling the core hole; either by emission of an Auger electron (Auger electron spectroscopy, AES) or by emission of a fluorescence photon (X-ray emission spectroscopy, XES). While the former is also a surface-sensitive probe due to the detection of electrons, the latter is a photon-in-photon-out technique which lends itself to study the surface near bulk and buried interfaces [29].

3.1.1 X-ray Photoelectron Spectroscopy (XPS)

XPS is highly surface-sensitive due to the short inelastic mean free path of photoelectrons that are emitted from the solid. For XPS, Al K_{α} (1486.6 eV) or Mg K_{α} (1253.6 eV) are the common photon energies of choice in a lab environment. XPS, also called “Electron Spectroscopy for Chemical Analysis” (ESCA), is an electron spectroscopic method which uses X-rays to knock electrons out of inner-shell orbitals. The kinetic energy (E_{kin}) of these photoelectrons is determined by the energy of the X-ray radiation ($h\nu$) and the electron binding energy (E_{bin}) as given by:

$$E_{kin} = h\nu - E_{bin} \quad (\text{work function neglected}) [31] \quad \dots\dots\dots(1)$$

The energy of the photoelectrons leaving the sample is determined using a Concentric Hemispherical Analyzer (CHA). This gives a spectrum with a series of photoelectron peaks, as the example in Figure 3-2 illustrate. The figure shown is the survey spectrum of an as-introduced SiC sample surface. Thereby the binding energy scale was calculated according to equation (1) with $h\nu$ (Mg K_{α}) = 1253.6 eV. The binding energies of the peaks are characteristic for each element. For example, as the C 1s electrons have the binding energy of 280 eV, one can see a peak at that particular binding energy in the figure. The peak areas can be used to determine the composition of the material surface. The shape of each peak and its binding energy can be influenced by the chemical state of the emitting atom. Hence, XPS can provide chemical bonding information as well. XPS must be carried out under ultra-high vacuum (UHV) conditions.

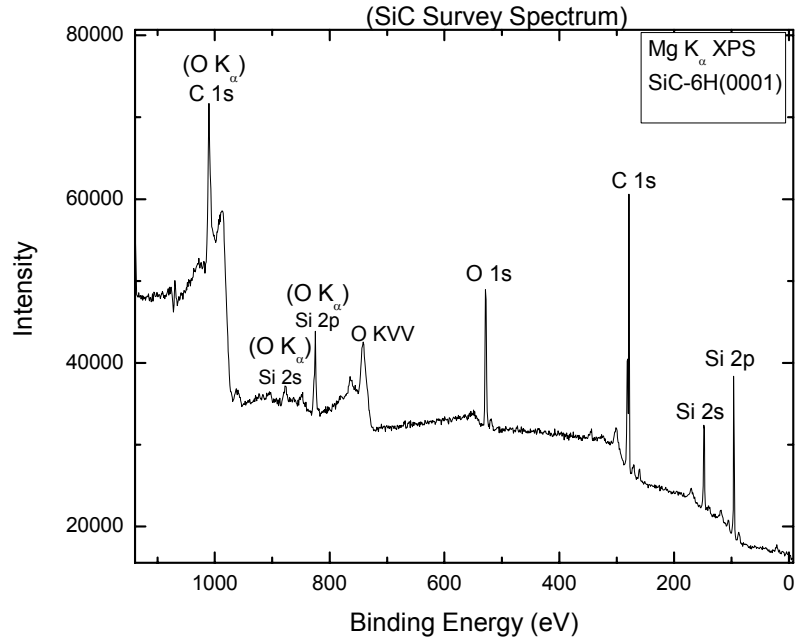


Figure 3-2 SiC survey spectrum.

The impurity, oxygen present on the anodes of the X-ray source (explained later) also takes part in the excitation of the sample. As a result, the peaks (e.g., C 1s, Si 2s, and Si 2p) below the excitation energy of oxygen (543 eV) show up once again in the survey spectrum, represented as O K_α in the above spectrum. Those peaks appear at a binding energy which is higher than its true one by the difference of the photon energies of Mg K_α and O K_α.

3.1.2 Ultraviolet Photoelectron Spectroscopy (UPS)

Ultraviolet light is shone at the sample using a Helium lamp emitting at 21.2 eV (He I radiation) or 40.8 eV (He II radiation). The low photon energy in UPS means that deep core electron levels can not be excited and only photoelectrons emitted from the valence band or shallow core levels are accessible [32]. However, due to the lower inherent line width, the spectral resolution for UPS is much higher than for XPS. UPS can also be used

to identify molecular species on surfaces by analyzing the valence bonds of the molecules. Angle-resolved UPS can be used to determine the band structure of the material under investigation. Furthermore, the secondary electron cutoff in UPS spectra can be used to determine the work function.

3.1.3 Auger-Electron Spectroscopy (AES)

As said before, X-rays can knock electrons out of inner-shell orbitals in an atom. These excitations cause core electrons from atoms contained in the sample to be ejected, resulting in a photoelectron and an atom with a core hole. The atom then relaxes via electrons with a lower binding energy relaxing into the core hole. The energy thus released can be converted into an X-ray or used to emit an additional electron. This electron is called an Auger electron. After the emission of the Auger electron, the atom is left in a doubly ionized state. The energy of the Auger electron is characteristic of the element that emitted it, and can thus be used to identify the element. Furthermore, it gives information about the local chemical structure of the emitting atom. As in the case of XPS, the short inelastic mean free path of Auger electrons in solids ensures the surface sensitivity of AES [32].

3.2 Instrumentation

The apparatus at UNLV, shown in Figure 3-3, mainly consists of four connected UHV chambers, namely an analysis chamber, a preparation chamber, a distribution chamber, and an ECR plasma etching chamber. For the work in this thesis, only the first two chambers are considered here.

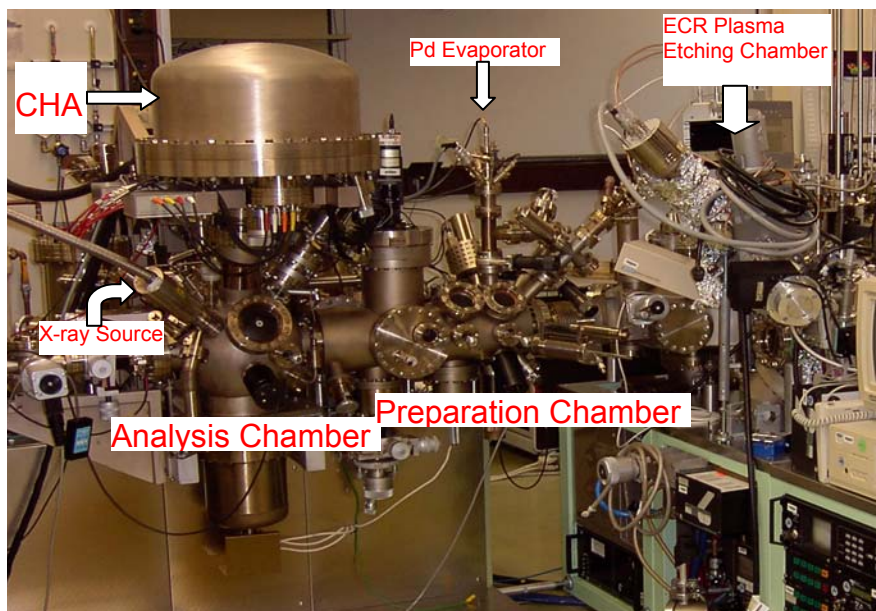


Figure 3-3 Picture of the ESCA in the Chemistry Dept., UNLV

The analysis chamber contains the X-ray source, UV source, sample manipulator, and a concentric hemispherical analyzer (CHA), which will be discussed in detail below. The preparation chamber is the chamber where the sample surface can be cleaned and/or modified by sputtering and annealing. Also, metal evaporation onto the sample can be done here. It is the intermediate chamber that the sample passes while transferring from the loadlock (the chamber from where the sample can be introduced into the system) to the analysis chamber.

3.2.1 Ultra High Vacuum (UHV)

UHV conditions are generally regarded as being in the region below 10^{-9} mbar (~ 750 pTorr). UHV is needed for surface science experiments as molecules in the ambient will adsorb on a surface and change its properties. At a pressure of 10^{-6} mbar, for example, a monolayer of gas molecules will form on the surface in about 1 second (assuming that every molecule to strike the surface sticks to the surface) [31]. This is

clearly not enough time to do an experiment. However, at UHV pressures, which are a factor 1000 and more lower in pressure, several hours of experiments can be performed before the sample surface is significantly degraded.

In order to achieve UHV, some special procedures are needed. Initially, the vacuum chamber is pumped down to 10^{-2} mbar using a rotary pump. Then, the chamber is pumped down to about 10^{-8} mbar using oil diffusion pumps. At this stage, the vacuum chamber is enclosed in an insulated tent and “baked” to a temperature of about 150° Celsius for 24 – 48 hours. After cool down to room temperature, the chamber should have a pressure in the UHV region. The process of baking removes residual molecules, in particular water, which are adsorbed on the inside chamber walls. These molecules slowly desorb from the chamber wall surfaces, and if the chamber was not baked, several months would have to pass before the chamber achieves UHV conditions.

3.2.2 Sample Handling

Sample introduction into the analysis chamber is done by a series of successive transfers. The sample sits on a metal stub which is placed at atmospheric pressure onto a holder on a trolley in a loadlock chamber. Following evacuation, the sample is transferred, first from the loadlock to the preparation chamber, and then from the latter into the analysis chamber with the help of a moving cart. This is achieved by a sequence of openings and closings of intervening gate valves, and of mechanical transfers from one trolley to another and then onto the sample manipulator. The transfer is carried out with bellows-sealed stub grips called ‘wobblesticks’. The highly flexible bellows allow a large amount of both angular motion and axial translation motion of the central shaft, although not, of course, rotational motion. A spring clip on the fork grips the sample stub firmly.

Once the sample is transferred into the analysis chamber, it needs to be positioned accurately for analysis by means of a manipulator. It provides X and Y lateral motions of +/- 12.5 mm and a Z translation motion of 50 mm. These motions are possible via a highly flexible all-welded bellows welded to the flange by which the manipulator is fitted to the system. Axial rotation through the full 360° is driven through an offset knuckle joint, also operating through a flexible bellow. Another option available is tilt, which alters the angle of the shaft inside the driving head [31].

3.2.3 Sample treatment

Because photoelectron spectroscopy, as mentioned above, is a surface-sensitive probe, it is important to have well-defined and clean surfaces throughout an experimental series. Surface cleanliness can be judged only by the techniques available in the analysis chamber, in our case in particular by monitoring the intensity of oxygen-related signals.

Heating alone will produce clean surfaces on a few materials but is in general inadequate unless used in association with a second technique. The problem is that the balance between desorption from and segregation of impurities to the surface in certain temperature ranges is characteristic of the material and of the impurity. The segregating contaminants must therefore be removed in some other way, and by far the most universally used method of doing that is by noble gas ion bombardment (“sputtering”). Ions, usually of argon, with energies chosen between 50 eV and 5 keV, are directed at the surface. Energy is exchanged with atoms in and near the surface as a result of successive collisions between the incident ions and the sample atoms in rest positions, as well as involving displaced atoms with excess energy, resulting in a cascade process that causes ejection of atoms and clusters from the surface. The surface is therefore eroded by loss of

material, the process of erosion being termed “sputtering”. In sputtering, the ions are produced in and directed and focused by an ion gun.

The best method of preparing a clean surface is a series of consecutive heating and ion bombardment steps, so that contaminants segregating or adsorbing to the surface in a heating cycle are removed in a bombardment cycle. The process has to be continued for as many cycles as are necessary either to remove all contaminants from the sample completely or, if that is not practical, to remove them from a certain depth in the sample by a careful choice of temperature and of bombardment conditions. Likewise, the annealing step will minimize the structural surface damage inflicted by the sputtering cycle, as can be monitored by techniques that are sensitive to surface structure (e.g., Low-Energy Electron Diffraction – LEED).

3.2.4 X-Ray Source

The interaction of a photon with a core level electron is given by [31],

$$E_k = hv - E_b - e\Phi$$

where

E_k = kinetic energy of ejected photoelectron w.r.t. the vacuum level

hv = characteristic energy of X-ray photon

E_b = binding energy of the core level w.r.t. the Fermi level

$e\Phi$ = work function term

From the above equation, it is evident that the line width of E_k will depend on the line width of hv . Furthermore, the lifetime broadening of the core level plays an important role (a so-called “final state effect”) via Heisenberg’s uncertainty principle. In XPS, chemical information is extracted by a detailed analysis of individual elemental spectra, including resolution of contributions from the various chemical states present, from

which it follows that the best energy resolution should be used compatible with the signal-to-noise ratio in the particular spectrum.

Generally, X-rays are generated in a material by bombardment with electrons of sufficient energy. For a particular X-ray line, photon emission starts at the ionization threshold of the core level involved and increases rapidly as the electron energy is increased, eventually saturating at some energy much higher than the threshold. For optimum sensitivity in analysis at a chosen energy resolution, the photon flux on the sample surface should be maximized; since the flux is directly proportional to the electron current bombarding the anode, as high a bombarding current should be used as the source will withstand (in our case, the X-ray source can be operated at up to 300 W for Mg K_{α} and 600 W for Al K_{α}). Since the flux irradiating the sample varies inversely as the square of the distance from the anode to the sample surface, it is essential to place the sample as close to the anode as all other constraints will permit.

In our experimental setup, the end of the copper anode has two angled faces, on one of which a film of aluminum is deposited and on the other a film of magnesium. There are two filaments, one for each anode material. Each filament and the surrounding shields are at ground potential, and a high accelerating potential of up to +15 kV is applied to the anode. With careful design of shields and of positioning of the semi-circular filaments, electrons from each filament bombard only the anode face nearer to it. X-rays generated in the bombarded face then pass out through an aperture in the surrounding cylindrical shield, covered with a thin sheet of aluminum foil. The aluminum foil is necessary in order to screen the sample from stray electrons, heating effects and any contamination originating in the source. Switching from Mg K_{α} to Al K_{α} radiation and back again is

simple and can be done in a couple of minutes. With possible maximum power dissipation up to 600 W and with such a compact design, heat must be removed from the anode quickly and efficiently, which necessitates a forced flow of water at high pressure [31].

3.2.5 Concentric Hemispherical Analyzer (CHA)

The CHA consists of two metal hemispheres (Figure 3-4). One hemisphere is being shaped concave, and the other convex. They are arranged such that their centers of curvature are coincident. Different voltages are placed on each hemisphere such that there is an electric field between the two hemispheres. Electrons are injected into the gap between the hemispheres. If the electrons are traveling very fast, they will impinge on the outer hemisphere. If they are traveling very slowly, they will be attracted to the inner hemisphere. Hence only electrons in a narrow energy region (called the pass energy) succeed in getting all the way through the hemispheres to the detector. A series of lenses are placed before the CHA. The lenses enable two operating modes - Constant Retard Ratio (CRR), or Constant Analyzer Energy (CAE). In the CRR mode, the electrons are slowed down by an amount which gives a constant ratio of the electron energy to be analyzed. That is, if the retard ratio is 10, and 1000 eV electrons are to be detected, then the electrons will be decelerated to 100 eV, and the pass energy will be set to 100 eV. In the CAE mode, the pass energy is fixed. Hence if the pass energy is 50 eV, then electrons of 1000 eV will have to be retarded by 950 eV in order to be detected. The CRR mode gives constant resolving power and the CAE mode gives constant energy resolution. For our XPS spectra, we have consistently used the CAE mode [31].

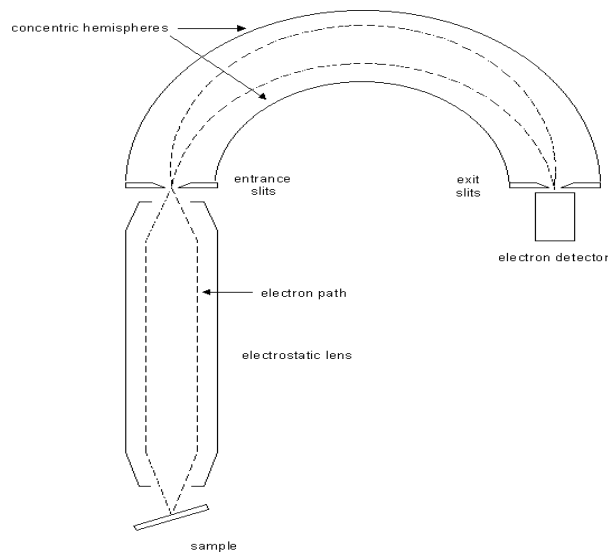


Figure 3-4 Concentric Hemispherical Analyzer (CHA) [32].

3.2.6 Electron detector

Multi-channel plate electron multipliers are used to count the individual electrons arriving at the detector. These consist of a three chevron-mounted plates with 256x256 channels, through which an incoming electron pulse is amplified by using an overall acceleration voltage of 4 kV. A resistive anode set-up allows the detection of the local position of the electron pulse, and a custom-written software integrates over this two-dimensional intensity image, taking the shape of the iso-energy surface into account. The output of the software is thus a spectrum of intensity vs. kinetic energy [33].

3.2.7 E-beam metal evaporator

The metal evaporator is an evaporator for small and medium quantities of many materials in the temperature range of 400K to 3100K. E-beam evaporation uses an electron beam to heat a source. Electrons are generated with a heated filament and are accelerated by several kV. The electron current is small, typically around 100 mA. The material for evaporation is either placed in a crucible or evaporated directly from a wire

of the desired material (as was done in our case of Pd). An integrated flux monitor allows an in-situ deposition control. Water-cooling ensures negligible outgassing during operation.

A sketch of the metal evaporator and its components is shown in Figure 3-5:

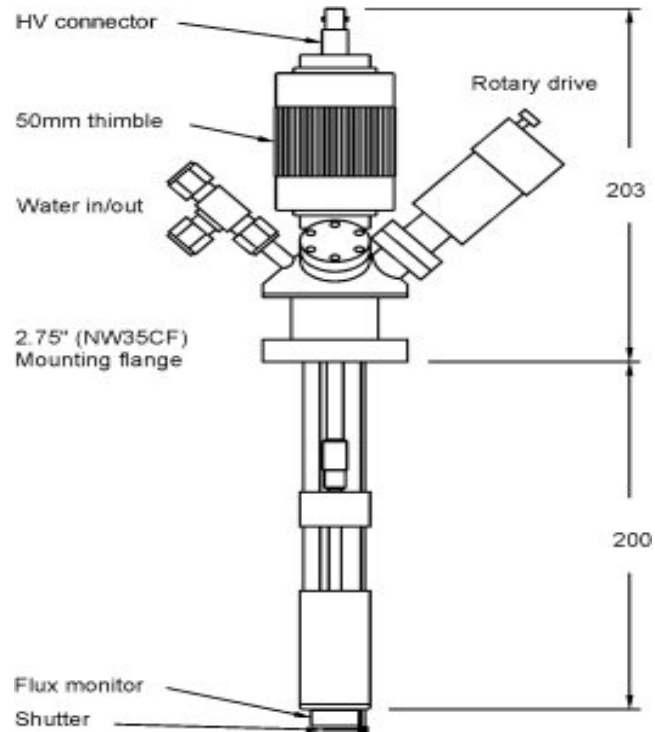


Figure 3-5 The e-beam metal evaporator and its various parts [34].

CHAPTER 4

RESULTS AND DISCUSSIONS

Three experimental series of Pd/6H-SiC(0001) interfaces were prepared under controlled conditions in an ultra-high vacuum environment and studied using XPS and UPS, respectively. In the first experimental series, the formation of the interface between a thin film of evaporated Pd and a well-ordered single crystal 6H-SiC(0001) surface at room temperature was investigated (Si-terminated 6H-SiC(0001) single crystals were purchased from Mateck, Jülich, Germany). In order to gain more directly applicable information about SiC layers in TRISO particles, two other experimental series (series 2 and series 3) were prepared. In these series, the SiC surface was cleaned and structurally disordered by extensive Ar⁺-ion sputtering with 2 keV ions in order to mimic the fact that TRISO SiC layers are not single-crystalline. The Pd layer thickness was then successively increased, and each step monitored by XPS and UPS. For series 2, the sample was kept at room temperature during deposition, whereas for series 3, it was heated to the currently highest attainable sample temperature in our system (approx. 800° C).

4.1 Experimental series 1

The survey spectrum of an as introduced SiC of this series is shown in Figure 4-1. Being an uncleaned sample, many adsorbates were present on the SiC surface (O 1s and F 1s). Since the sample was smaller than the probing area of the electron analyzer, also Ta signals can be found (Ta was used to fix and contact the sample). The peaks measured with O K_{α} are due to oxygen contaminations on the X-ray anode resulting in an O K_{α} line in the excitation spectrum. The Auger peaks, O KVV, F KLL, and C KVV can also be seen.

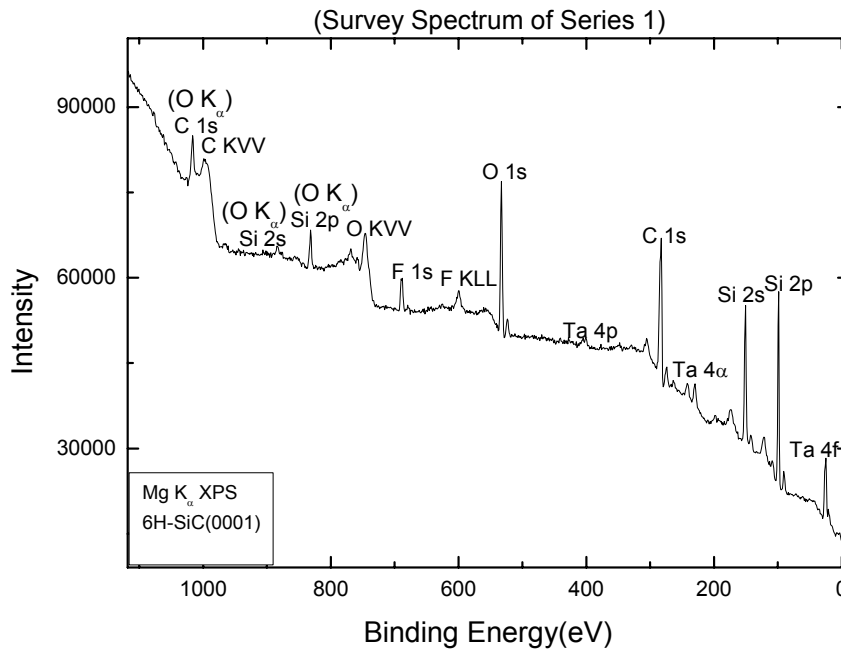


Figure 4-1 Survey spectrum of the as-introduced SiC sample of series 1.

In contrast to the two experimental series discussed below, the 6H-SiC(0001) single crystal surface was now prepared to regain its single-crystalline structure and a high degree of lateral order at the surface, as evidenced by low-energy electron diffraction

(LEED). This was done by various sputtering and annealing steps. After the single crystalline surface was prepared, a thin layer of Pd was deposited on SiC and monitored using XPS. A rough estimate based on the attenuation of the Si 2p signals suggest an approximate thickness of a monolayer.

Figure 4-2 represents the C 1s core level before and after the deposition of the thin Pd layer. As can be seen from the included peak fit analysis using Voigt line shapes and a linear background, two chemically different carbon species (282.8 eV, 284.3 eV) exist at the clean and uncovered SiC(0001) surface, which we ascribe to a bulk (a) and a surface species (b), respectively. After the Pd deposition, three different carbon species (282.4 eV, 284.0 eV, and 286.0 eV) exist which are ascribed to (a) a bulk species, (b) an interface species, and (c) a reacted species. The latter is possibly due to a diffusion of Pd into the region near the interface (and presumably further into the bulk of SiC). In parallel, the Si 2p core levels (shown in Figure 4-3) also show the existence of two different Si species, both before and after the interface formation. Again, these are ascribed to a surface and a bulk component before formation of the interface and to an interface and a bulk component after Pd deposition.

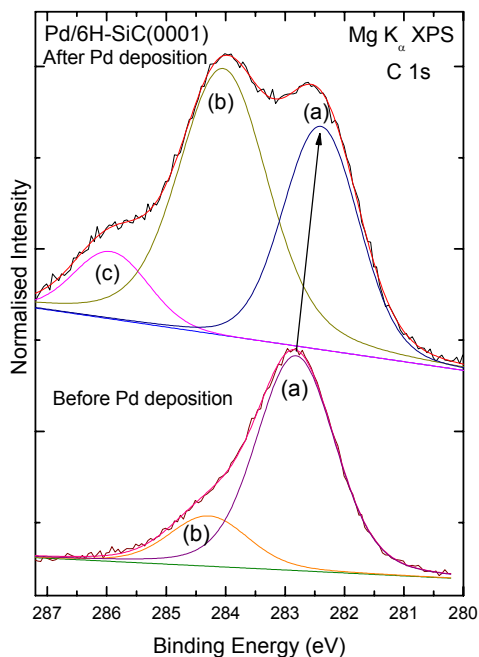


Figure 4-2 Peak fit analysis of the C 1s peaks before and after Pd deposition on 6H-SiC(0001). The C 1s Species shown are (a) a bulk species, (b) a surface species before Pd deposition and (a) a bulk species, (b) an interface species, and (c) a reacted species after Pd deposition.

In both cases, there is an upward shift (i.e., to lower binding energies) of all electronic levels, as indicated by the arrows in Figures 4-2 and 4-3. This is presumably due to a change in surface band bending of the SiC substrate upon formation of the metal/semiconductor interface.

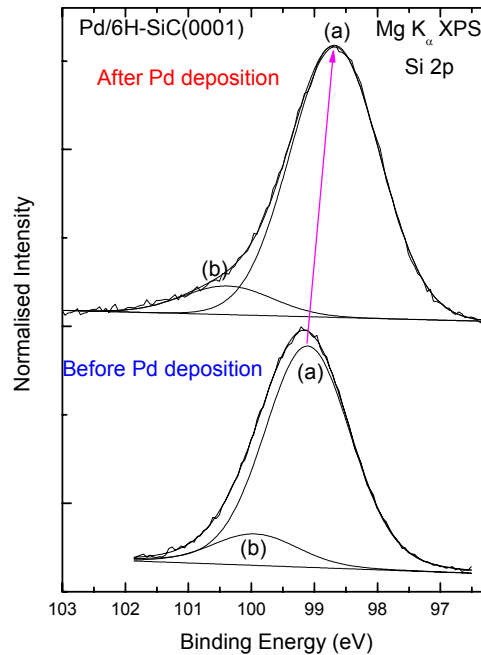


Figure 4-3 Peak fit analysis of Si 2p. Before Pd deposition (a) a bulk species and (b) a surface species are found; after Pd deposition, (a) a surface species and (b) an interface species are shown.

4.2 Experimental series 2

As TRISO SiC layers are not single-crystalline, a structurally disordered SiC substrate surface was prepared in this series by extensive Ar^+ -ion sputtering cycles with 2 keV ions. The metal/semiconductor interface was formed at room temperature where the Pd layer thickness was successively increased. After each deposition step, the sample was investigated by XPS and UPS.

Figure 4-4 shows a sequence of XPS survey spectra from this series. As labeled on the right hand side, the spectra correspond to the as-introduced SiC single crystal surface (bottom spectrum), the sample after each Ar^+ ion sputter-cleaning (and roughening) cycle, and after each Pd deposition step. As indicated by the blue oval, the impurities on

the sample surface (as evidenced by O 1s) are reduced after each sputtering cycle. After four successive sputtering cycles, only a very small residual oxygen signal could be detected. The red oval indicates the increase in the intensity of Pd 3d after each successive Pd deposition step. In parallel, the C 1s and Si 2p signals decrease due to attenuation in the Pd layer covering the SiC substrate, as indicated by the green and black ovals, respectively. The peaks above the binding energy of ~ 800 eV are from O K_{α} excitation (explained above).

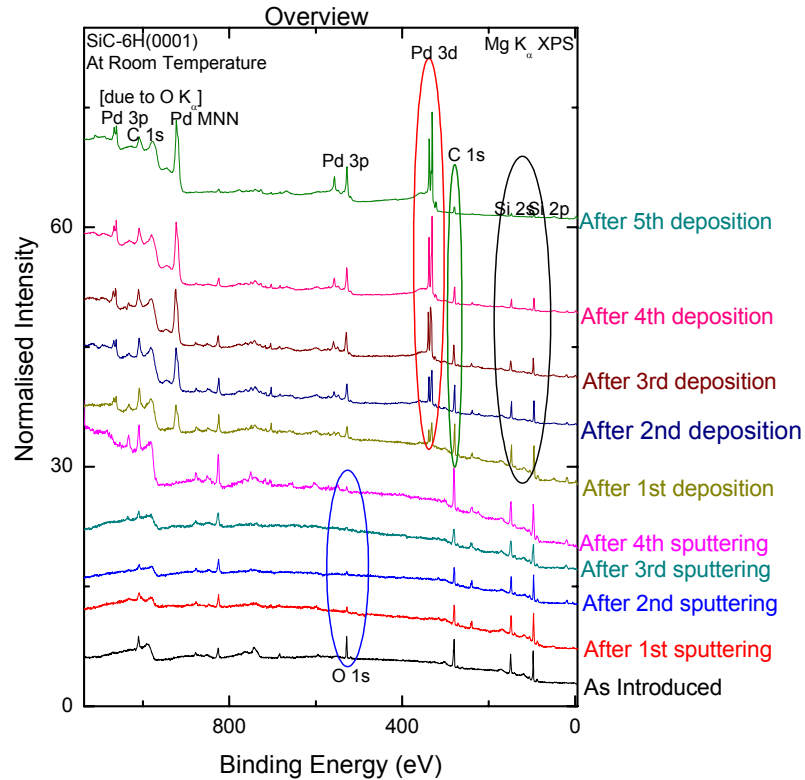


Figure 4-4 Sequence of survey spectra from series 2.

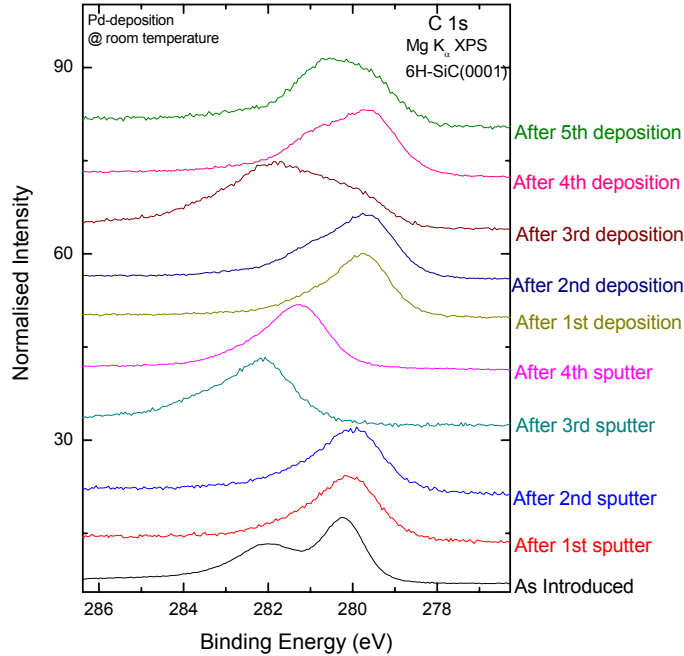


Figure 4-5 C 1s XPS spectra from series 2.

For the spectra measured after the 3rd and 4th sputtering cycle, the sample exhibited an improper electrical contact, such that the spectra are shifted to higher binding energies due to charging of the sample. Likewise, the spectrum after the 3rd deposition step appears to be obscured, most likely due to sample misalignment. These spectra were then not included in the data interpretation.

Figure 4-6 shows the C 1s multi-spectra peak fit analysis. All peak fits in this work were performed using a Voigt line shape after the subtraction of a linear background. It features a peak that is a convolution of many interactions causing various broadening features based upon Lorentzian and Gaussian line shapes. The Gaussian component primarily describes the experimental line broadening, including the line shape of the Mg K_{α} excitation and the finite resolution of the electron analyzer. The Lorentzian part primarily describes the lifetime-broadening of the core level [34]. All spectra were fitted

simultaneously to be able to set common parameters between the different fits, in particular to obtain the same separation between the different species, the same line width, etc. This ensures that quantitative information about the emergence of new chemical species can be obtained.

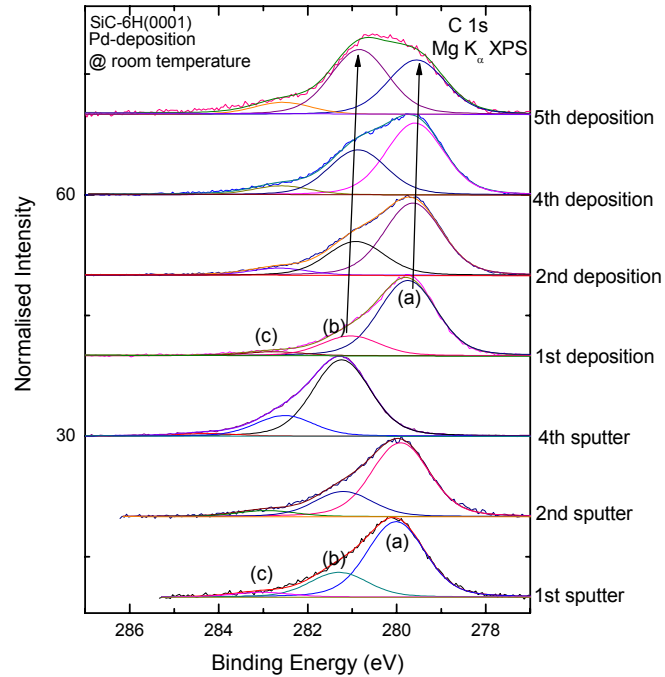


Figure 4-6 Peak fit analysis of the C 1s spectra.

As can be seen from the included peak fit analysis, three chemically different carbon species exist at the clean and uncovered SiC(0001) surface, and their intensity varies as a function of Pd deposition. The three carbon species are (a) a bulk species (at 279.5 eV in the topmost spectrum), as this peak is decreasing gradually in intensity after each Pd deposition step, (b) an interface species (at 280.8 eV in the topmost spectrum), as this peak is gradually intensified as a function of deposition, and (c) presumably adventitious carbon. The interface species (b) gets more prominent than the surface species (a) as a

function of Pd coverage. There is also a shift of species (a) and (b) towards smaller binding energies (indicated by the arrows in Fig. 4-6), most likely due to a long-range charge transfer (as is commonly found in the formation of Schottky contacts [38]), which indicates a change in surface band bending of the SiC substrate due to the formation of the metal/semiconductor interface (explained later).

The relative changes in the areas of the three C 1s species are shown in Figure 4-7. After depositing Pd, one can see a gradual decrease in the area of the C 1s surface species (a), while the areas of the two other peaks increase. This points towards an intermixing at the Pd/SiC interface.

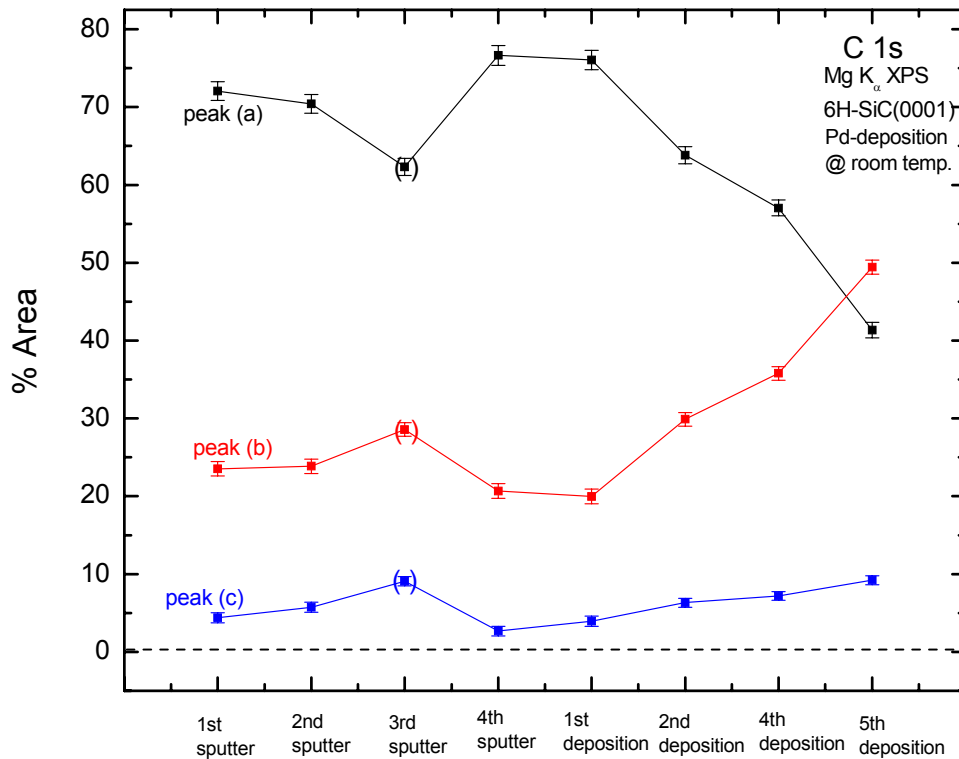


Figure 4-7 Area percentages of all three C 1s species of the second series.

Similarly, the Si 2p spectra of this series (shown in Figure 4-8) change significantly as a function of sample treatment. As in the carbon spectra, there is an emergence of an additional silicon structure after deposition (indicated by the oval).

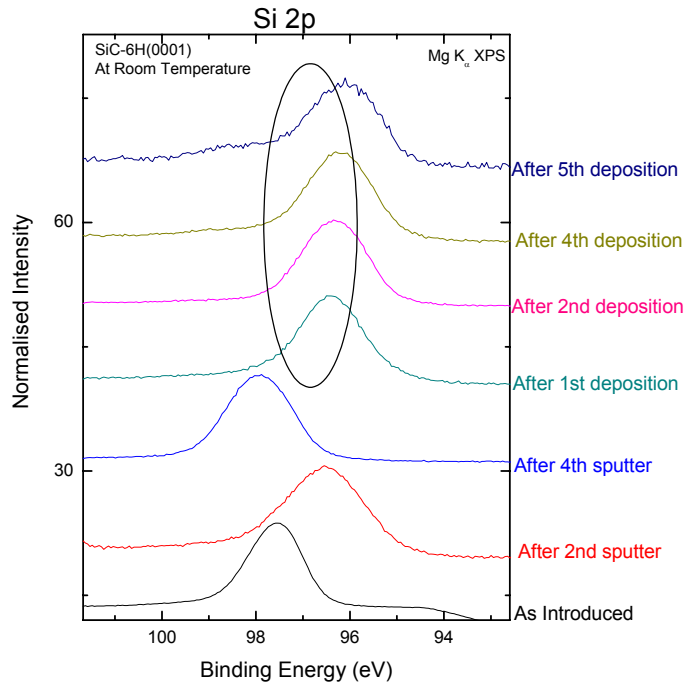


Figure 4-8 Si 2p XPS spectra, second series.

Figure 4-9 shows the peak fit of the Si 2p XPS spectra, which again were fitted simultaneously. Here in this work, for Si 2p, the fits are done by taking the spin-orbit splitting of the Si 2p levels into account. That is, for each species, a doublet (consisting of the Si 2p_{1/2} and 2p_{3/2} levels) was fitted with constant area ratio (1:2) and constant separation (2.24 eV). As in the case of the C 1s spectra, the spectra after the 3rd and 4th sputter step are shifted due to charging problems. As can be seen from the included peak fit analysis, the clean and uncovered SiC(0001) surface can be well described by a single peak duplet. To optimize the fit, a second (weak) species was included at approx. 100 eV.

The main peak is associated with the bulk species, while the weak shoulder can be attributed to some residual Si-O bonds, which is corroborated by peak (b) in the fit analysis of the earlier sputter steps (i.e., with a larger amount of residual O contamination at the surface). After Pd deposition, two species are clearly required to satisfactorily describe the spectra. They are ascribed to a SiC bulk species (a) and an interface species (c), as the interface species increases with increasing Pd coverage (which can be seen quantitatively in Figure 4-10). An alternative interpretation of the structure (c) could be based on an extrinsic (correlated) energy loss of the outgoing photoelectrons while passing through the Pd layer. There is a shift of species (a) towards smaller binding energies in a similar manner as seen in the C 1s spectra, which indicates a change in surface band bending of the SiC substrate due to the formation of the metal/semiconductor interface.

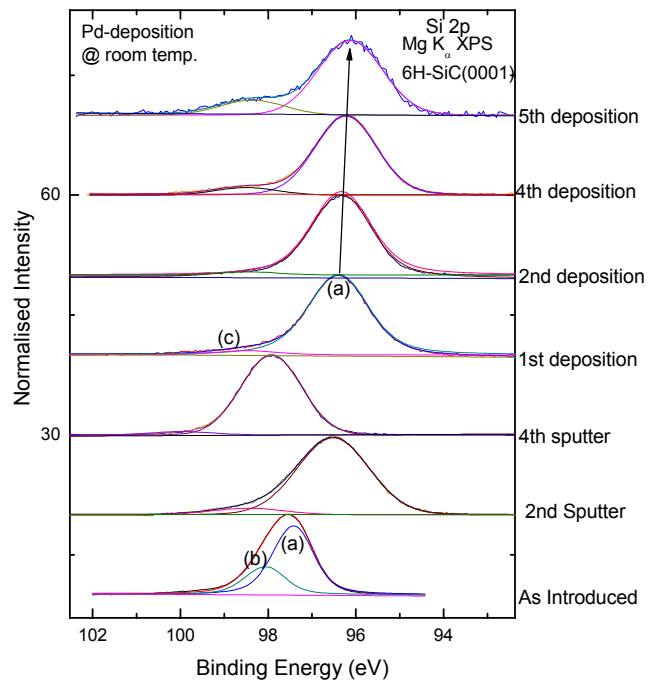


Figure 4-9 Peak fit analysis of the Si 2p spectra, second series.

The change in the area percentages of the Si 2p species is shown in Figure 4-10. After depositing Pd, there is a gradual decrease in the area of the bulk species (a) and an increase of the intensity of the interface species (or loss feature) (c).

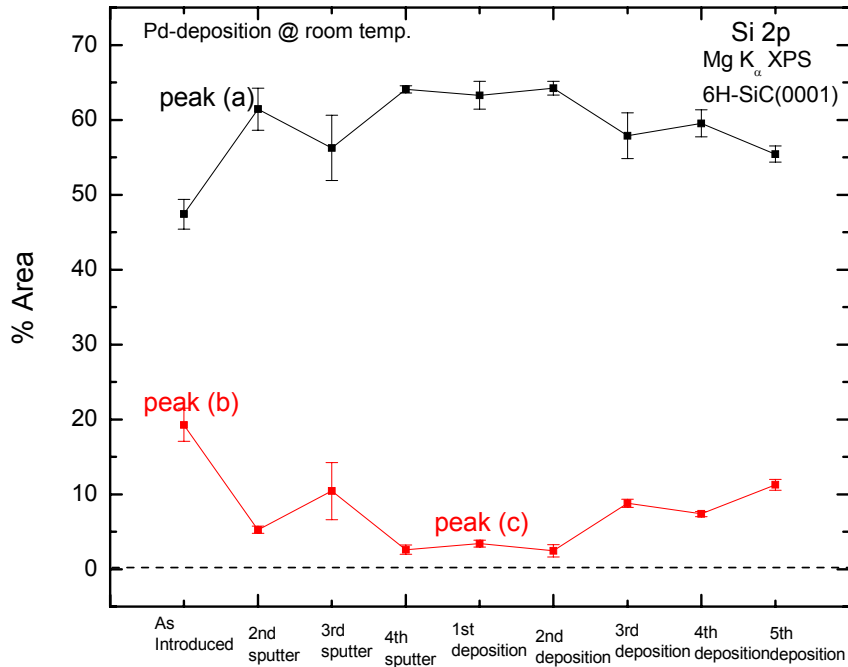


Figure 4-10 Percent area plot of the Si 2p species

Figure 4-11 shows the Pd 3d_{3/2} spectra as a function of deposition steps. After each deposition, the Pd 3d_{3/2} signal increases. Furthermore, the peak line shape is gradually getting asymmetric, as shown in Figure 4-12 by comparing the spectra from the thinnest and thickest Pd film. This asymmetry is ascribed to the increasingly metallic character of the overlayer (explained below).

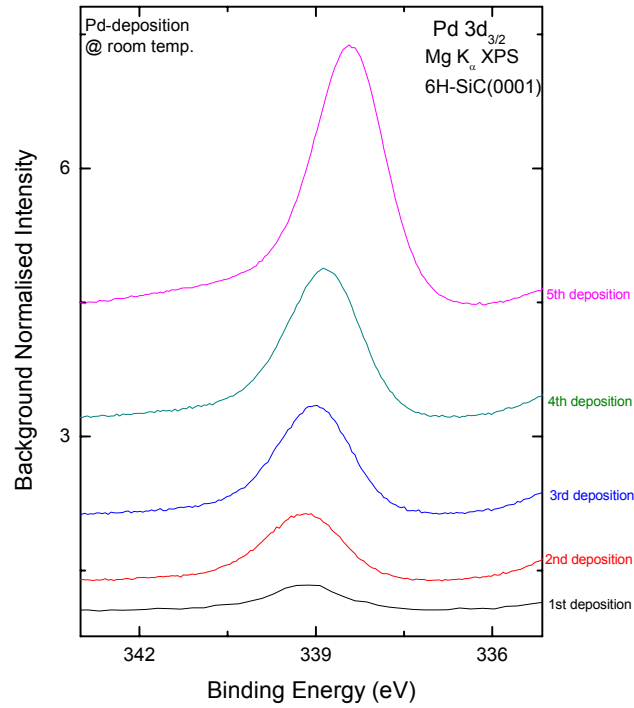


Figure 4-11 Pd 3d_{3/2} spectra as a function of deposition step

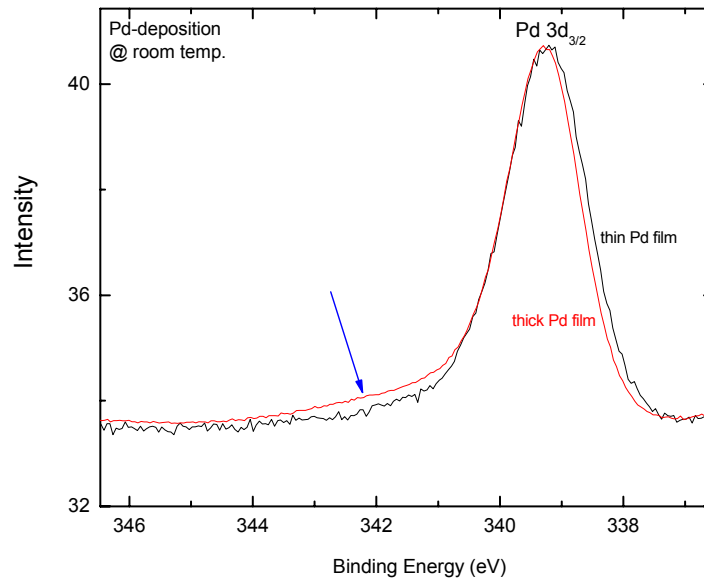


Figure 4-12 Comparison of Pd 3d_{3/2} peaks for the thickest and thinnest Pd film.

The arrow indicates the region of increased asymmetry of the lineshape for the thickest film, corresponding to an increased metallicity of the overlayer.

After the 1st deposition, only a thin layer of Pd is deposited and it may be deposited as individual islands on the surface. If this is the case, Pd atoms may be present in several different environments (such as Pd bonded to the SiC substrate, Pd with one Pd neighbor, with two Pd neighbors, etc.). Due to the large number of different environments in this case, the Pd 3d_{3/2} peak after the 1st deposition (thin Pd film) is broader than the peak after the 5th deposition (thick Pd film), as can be seen in Fig. 4-12. However, it is still symmetric due to the lack of metallic character in the confined Pd islands. Only for the thicker Pd films, the typical asymmetric line shape found for metals (Doniach-Sunjic) is observed. This asymmetry is induced by the possibility of very small energy losses of the outgoing photoelectron due to scattering processes that promote electrons from just below the Fermi energy to states just above the Fermi energy. Such losses give rise to a continuous shoulder of metallic photoemission peaks, as observed here. The findings thus indicate that the film is not yet metallic after the first deposition step (see also the discussion of the UPS spectra below).

As can be seen in the quantitative summary of the peak shifts mentioned above in Figure 4-13, the C, and Si levels are significantly pushed to lower binding energies after the first deposition step, and then gradually shift to even lower binding energies as a function of deposition. This indicates that there is a change in the band bending of SiC during the interface formation, which will be discussed in more detail below. Furthermore, we find a more pronounced decrease of the Pd 3d_{3/2} binding energy, which

is associated with the gradual formation of metallic regions on the SiC surface and the improved screening that is associated with larger metallic domains.

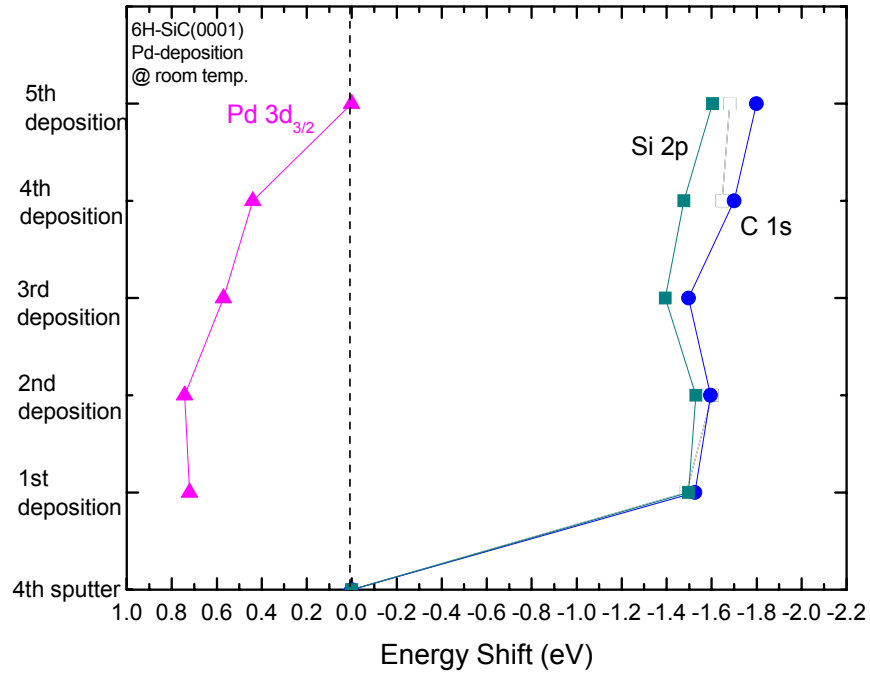


Figure 4-13 Relative binding energy change in the peak positions of C 1s, Si 2p, and Pd 3d_{3/2}.

Figure 4-14 shows the UPS survey spectra which show the secondary electron cutoff (SEC) region and the valence band (VB) region. The detailed SEC and the upper valence band are shown in Figures 4-15 and 4-17, respectively.

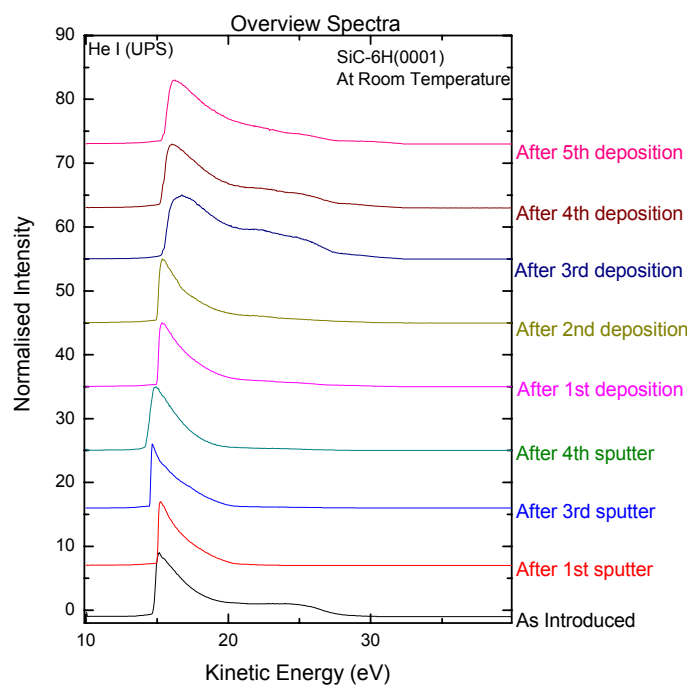


Figure 4-14 Sequence of UPS survey spectra for the second series, taken with a bias voltage of 15 V and not taking the work function of the electron analyzer into account.

From the SEC spectra, the work function of the sample at each step can be determined by a linear extrapolation of the leading edge and by evaluating the intersect with the baseline extrapolation. The derived values are shown in Figure 4-18 as a function of sputter treatment and/or Pd deposition. The work function increases gradually, indicating that the overlayer converts gradually from isolated Pd islands to metallic Pd areas. However, the absolute values found in our study are unexpectedly low, both for SiC (literature value: 4.8 eV [35]) and metallic Pd (literature value: 5.1 eV [36]). We suspect that this is due to a calibration problem. Nevertheless, relative changes are estimated to be accurate within 0.2 eV.

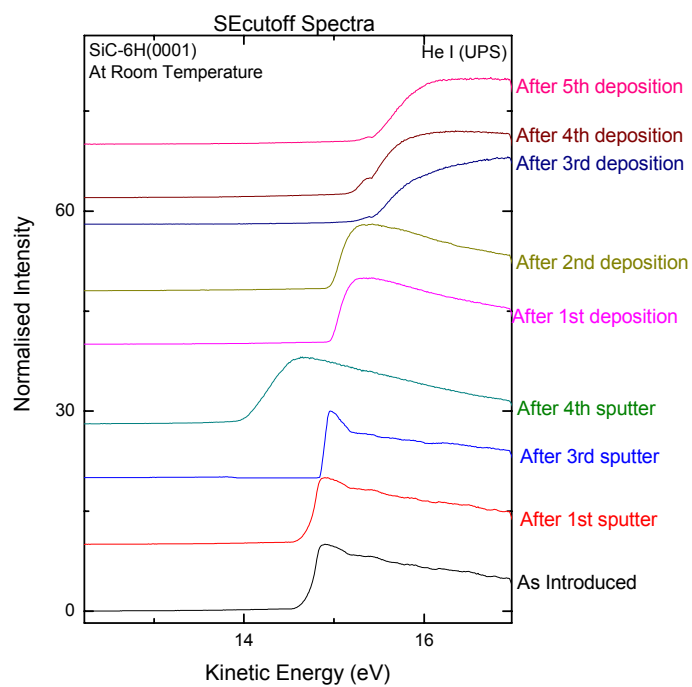


Figure 4-15 Secondary electron cut-off spectra of the second sample series.

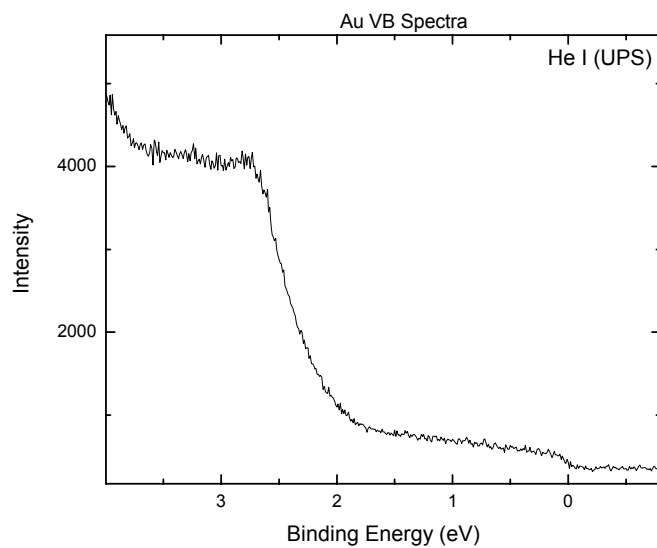


Figure 4-16 Au reference spectrum.

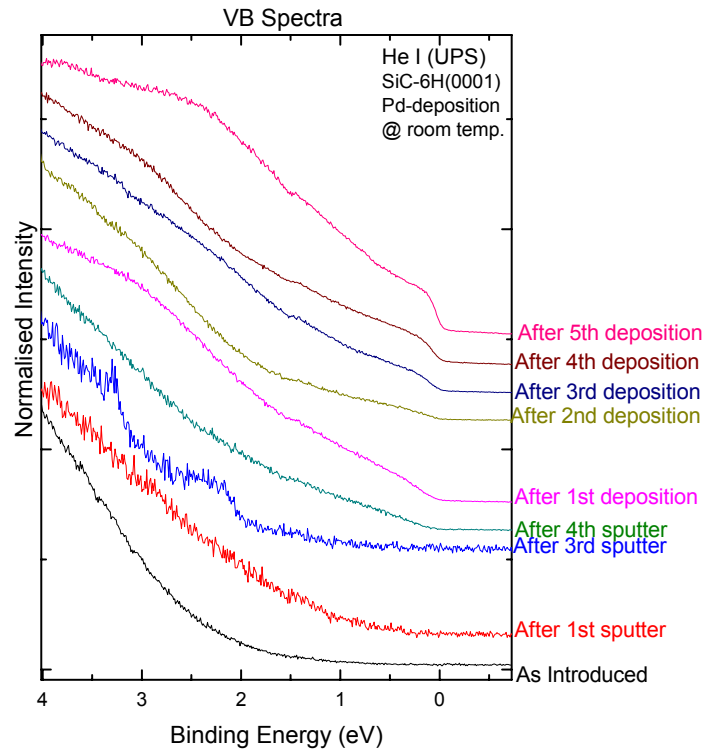


Figure 4-17 Upper valence band spectra of the second sample series

From the spectra of the upper valence band, the valence band maximum (VBM) can be determined by a linear extrapolation of the leading edge and by evaluating the intersect with the baseline extrapolation. As a function of sputter treatment, the VBM shifts upwards, i.e., to lower binding energies (as shown in figure 4-18). As the Pd coverage increases, a Fermi edge emerges between 32.05 and 32.15 eV (the Fermi energy is evaluated as the inflection point of the Fermi edge). The Fermi edge position of a Au reference sample, which was observed at 32.20 eV. This indicates that the Pd film increasingly gets a more “bulk-metallic” character throughout the deposition series.

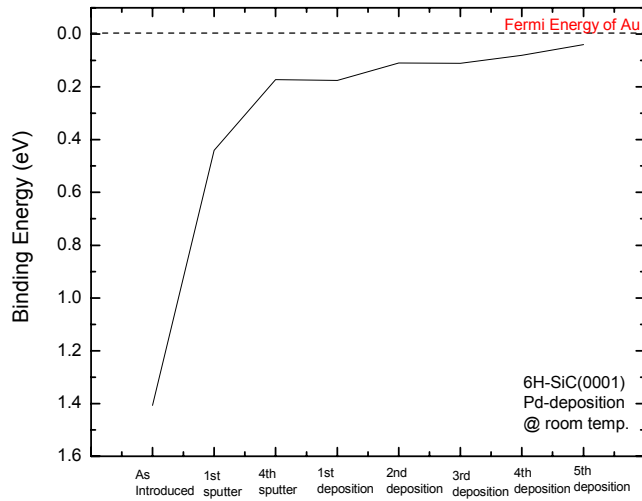


Figure 4-18 Position of the valence band maximum/Fermi edge for the second series.

Figure 4-19 is the plot of the work function of the sample at each step. As can be seen from the figure, the work function of the sample is increasing as Pd deposition starts.

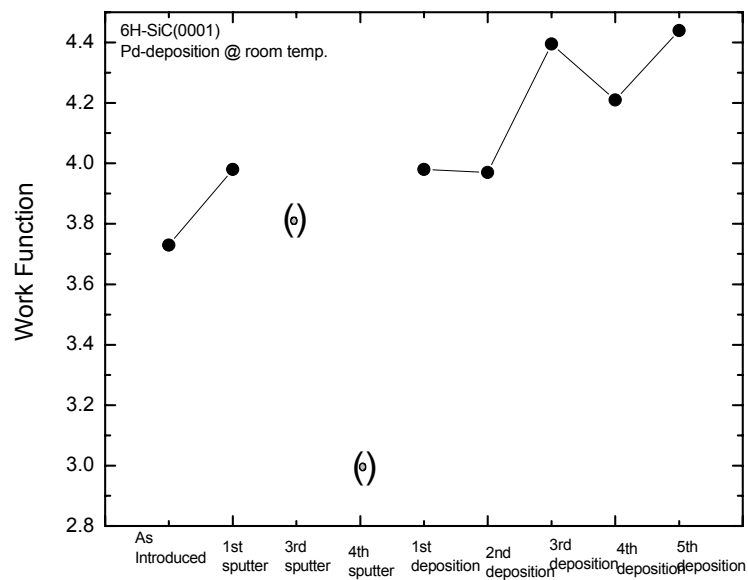


Figure 4-19 Work Function plot of the sample.

4.3 Experimental series 3

In order to make the investigation of the Pd/SiC-single crystal interface more directly applicable to SiC layers in TRISO particles, the sample in this series was not only structurally disordered by extensive Ar⁺-ion sputtering cycles with 2 keV ions, but the metal/semiconductor interface was furthermore also formed at elevated temperatures (approx. at 800°C, the currently highest attainable temperature in our system). As in the previous series, the Pd layer thickness was successively increased.

Figure 4-20 shows a sequence of XPS survey spectra from this series. The sample was cleaned before the Pd deposition by prolonged Ar⁺-sputtering, leading to an almost complete removal of the O 1s signal. As a function of deposition, we observe an increase of the Pd signals as well as an attenuation of the Si and C signals.

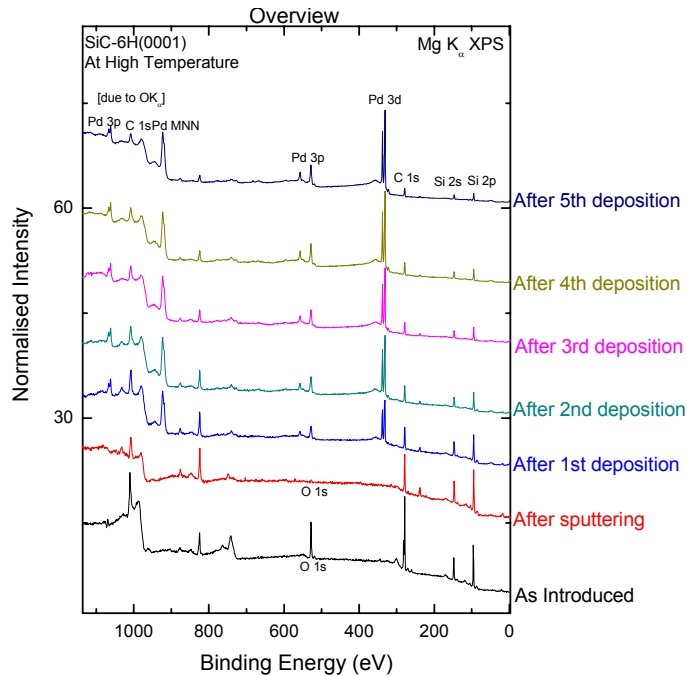


Figure 4-20 Sequence of XPS survey spectra of series 3.

Figure 4-21 shows a sequence of C 1s XPS spectra, obtained from this series, i.e., the interface sample grown at approx. 800°C substrate temperature. The spectra change significantly as a function of sample treatment. During the sputter treatment, adventitious carbon is removed, which can be seen by the absence of the peak at 282 eV in the spectrum following the sputter-cleaning.

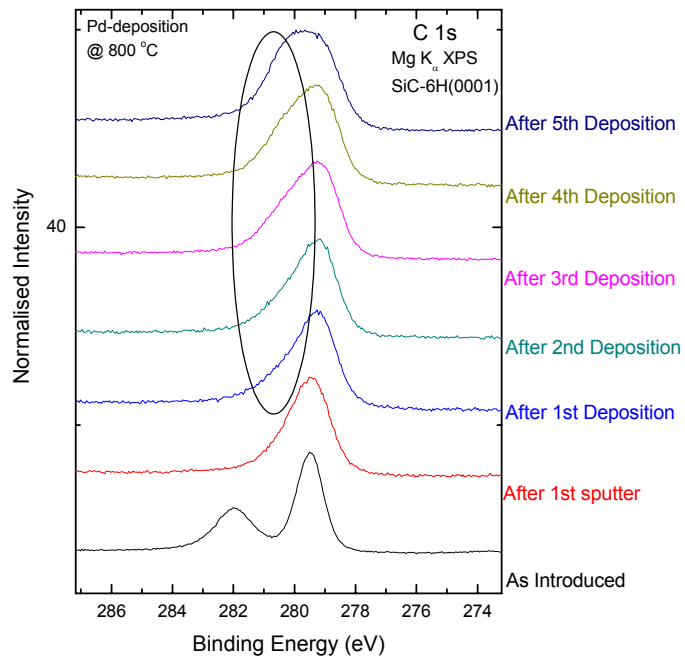


Figure 4-21 Sequence of C 1s XPS spectra.

During the Pd deposition, we find the emergence of an additional carbon species, as indicated by the oval in the above figure. In the topmost spectrum, we find a strongly different C 1s peak shape. The multi-spectra peak fit of C 1s is shown in Figure 4-22. At least two chemically different carbon species exist at the clean and uncovered SiC(0001) surface.

Upon deposition of Pd, two major effects are visible, first a shift of the main peaks (indicated by the arrows) towards smaller binding energies, most likely due to a change

in band bending, and second a variation in the relative intensities of the various C species.

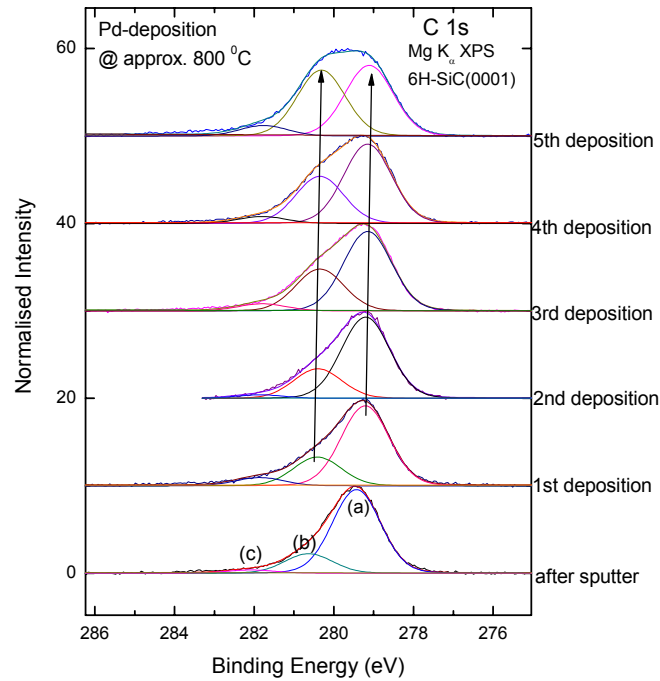


Figure 4-22 Peak fit analysis of C 1s spectra.

From the peak fit analysis, the three carbon species are ascribed to (a) a SiC bulk species (at 279.1 eV in the topmost spectrum), (b) an interface species (at 280.3 eV in the topmost spectrum), and (c) adventitious carbon. The species (a) is less dominant when compared with the species (b) and (c) after the deposition of Pd.

The relative change in the areas of the three C 1s species is shown in Figure 4-23. As also observed from series 2, after depositing Pd, there is a gradual decrease in the relative area of the bulk species of the C1s peak (a), whereas the relative areas of the other two peaks increase. This supports the interpretation that the interface species (b) is

dominating over the bulk species (a) after Pd deposition. This is most likely due to an intermixing at the interface.

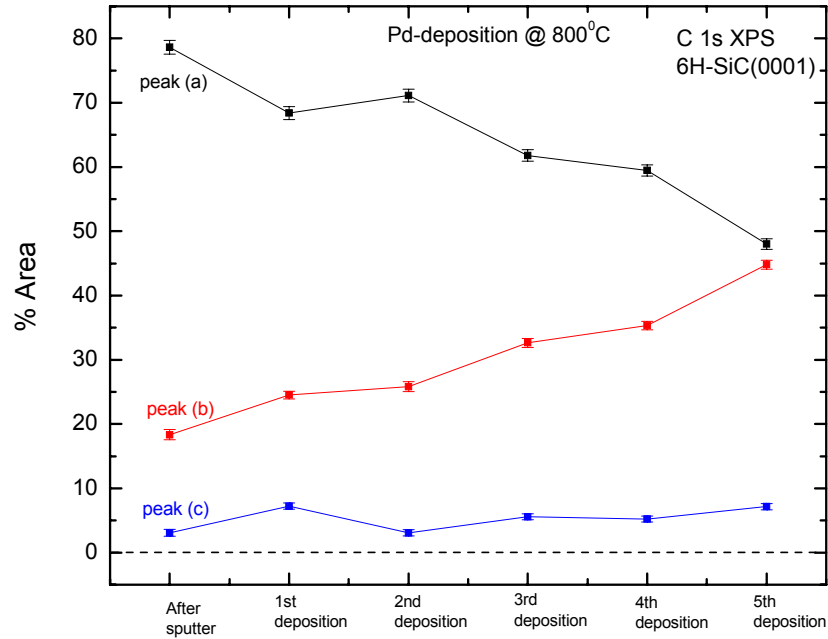


Figure 4-23 Area percentages of all three species of C1s, third series.

Similarly, the sequence of Si 2p spectra is shown in Figure 4-24. As the thickness of the Pd layer increases gradually, we find a shift of the Si 2p peak towards lower binding energies, which can best be seen in the peak analysis of the Si 2p spectra in Figure 4-25. There is an emergence of an additional Si 2p species after the deposition starts (indicated by the oval).

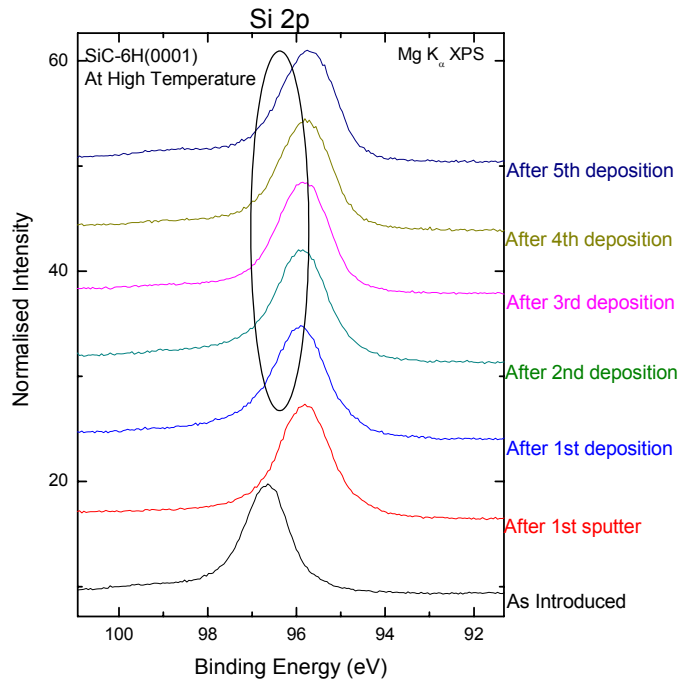


Figure 4-24 Si 2p XPS spectra, third series.

As can be seen from the included peak fit analysis in Figure 4-25, two species, (a) a bulk species and (b) a surface species, exist at the clean and uncovered SiC(0001) surface. After the final deposition step, three species, (a) a surface species, (c) an interface species, and (d) an additional species, which is interpreted as either an oxidized Si species or a loss peak, can be seen. There is a shift of the main peaks towards smaller binding energies in the similar manner as seen in C 1s spectra, which indicates a change in surface band bending of the SiC substrate due to the formation of this metal/semiconductor interface.

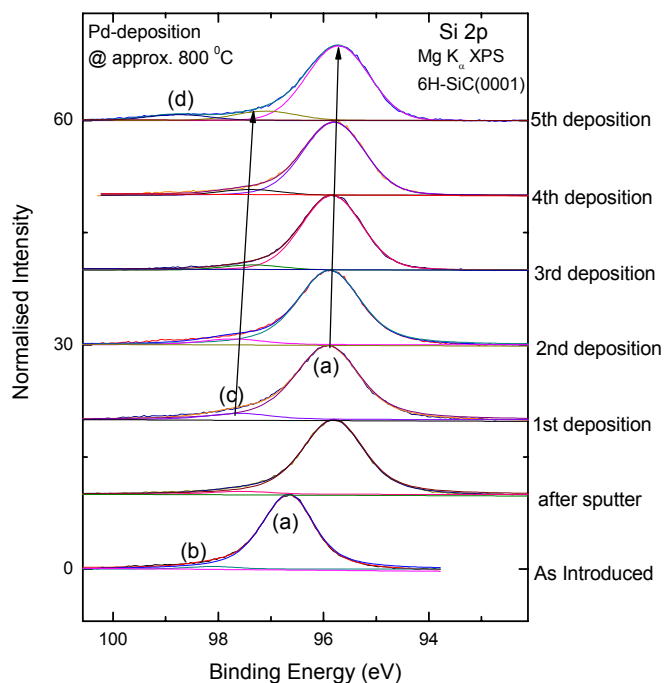


Figure 4-25 Peak fit analysis of the Si 2p spectra. Before Pd deposition, (a) bulk, (b) surface species; and after Pd deposition, (a) surface, (c) interface species are seen. An additional species (d) can also be seen after the last deposition step.

The relative change in the areas of the Si 2p species is shown in Figure 4-26. After depositing Pd, there is a gradual decrease in the area of the bulk species (a) and an increase in the intensity of the interface species (b). Figure 4-27 shows the Pd 3d_{3/2} spectra as a function of deposition steps. After each deposition, the Pd 3d_{3/2} signal increases. Gradually, the shoulder of the Pd 3d_{3/2} peak at higher binding energies increases (shown by the oval), indicating that the peak is getting asymmetric, i.e., towards a metallic line shape expected for bulk Pd.

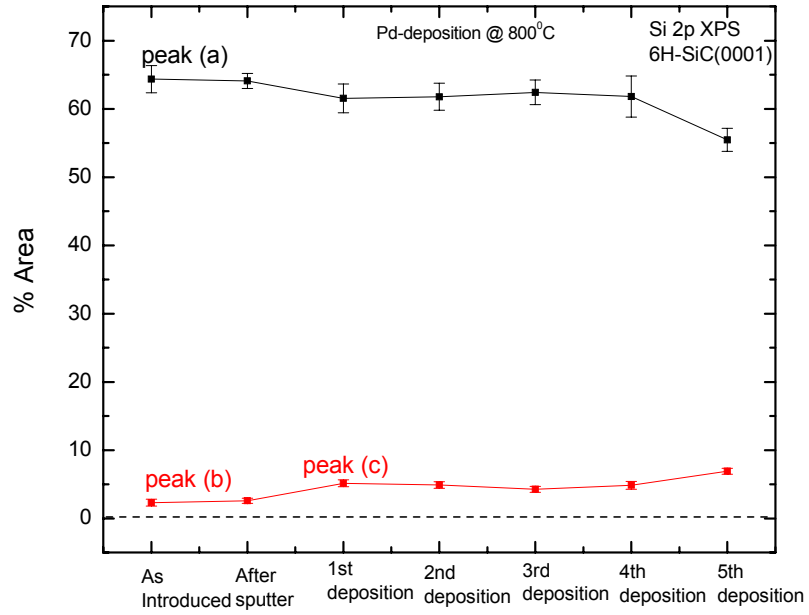


Figure 4-26 Percent area plot of Si 2p, third series.

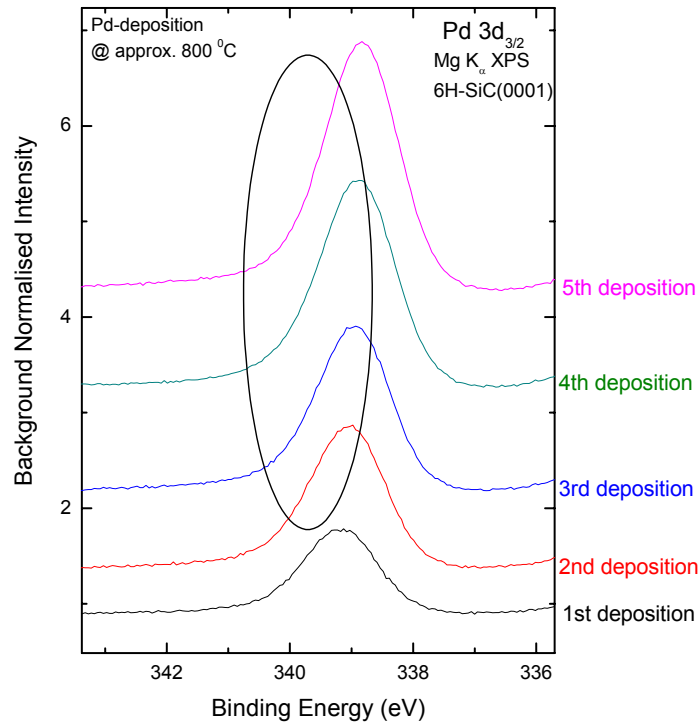


Figure 4-27 Pd 3d_{3/2} spectra as a function of Pd deposition.

As can be seen from Figure 4-28, the bulk species of all elements (C 1s, Si 2p, and Pd 3d_{3/2}) are gradually shifting upwards (i.e., to lower binding energies) as a function of deposition (note that, due to the nature of the simultaneous fit, all other species derived in the fits follow this trend). This indicates that there is a change in the band bending of SiC due to the formation of a Schottky barrier, as will be discussed below. Furthermore, we note that the behavior of Si and C is different for the first Pd deposition step: while the Si 2p levels shift downwards, the C 1s peaks shift upwards. This is a clear indication of a short-range chemical interaction that most likely transfers electronic charge from the Pd atoms to the Si atoms. Note that this effect does not appear to be present in the sample series prepared at room temperature (compare with Fig. 4-13).

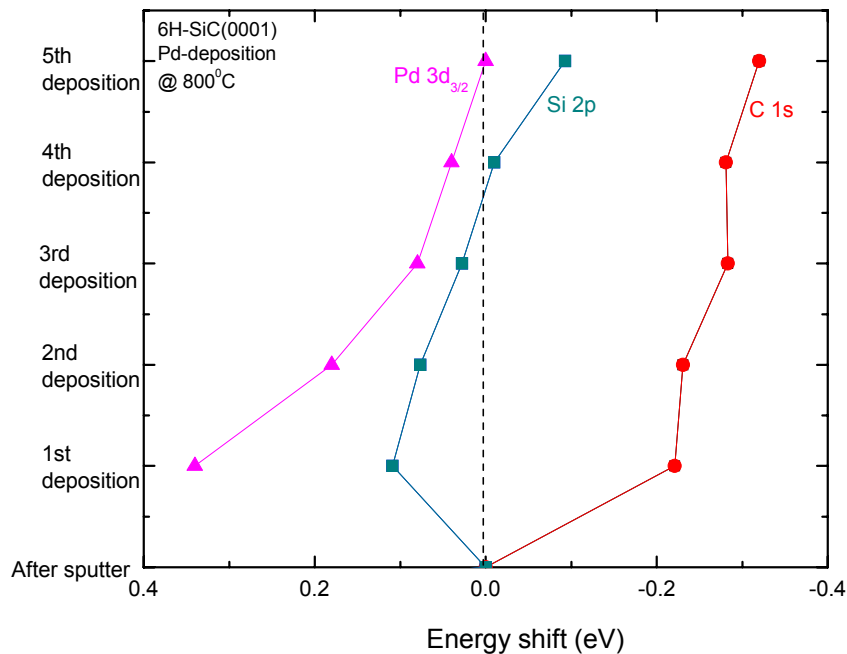


Figure 4-28 Relative change in the peak positions of C 1s, Si 2p, and Pd 3d_{3/2}.

Figures 4-29 to 4-31 show the UPS survey spectra, the secondary electron cutoff region, and the valence band maximum region, respectively. From the SE cutoff spectra, the work function of the material at each step can be determined (shown in Figure 4-33), as explained above.

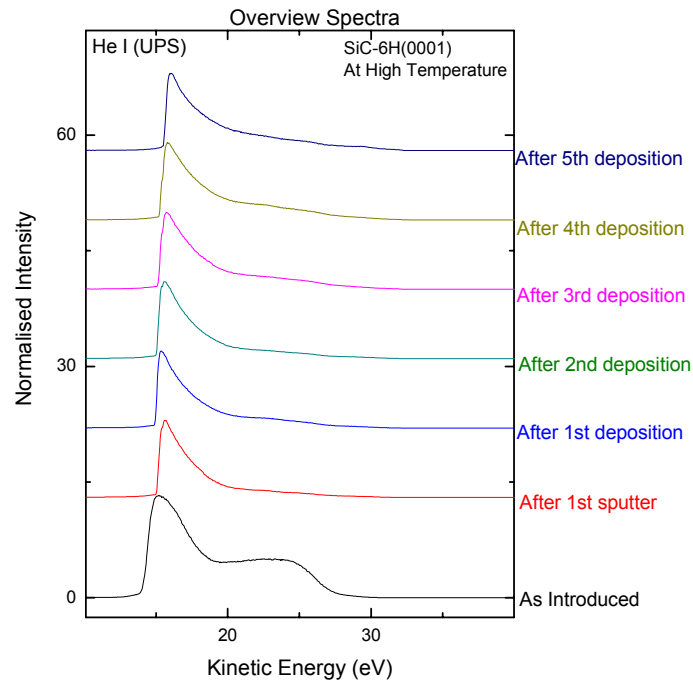


Figure 4-29 Sequence of UPS survey spectra for the third series, taken with a bias voltage of 15 V and not taking the work function of the electron analyzer into account.

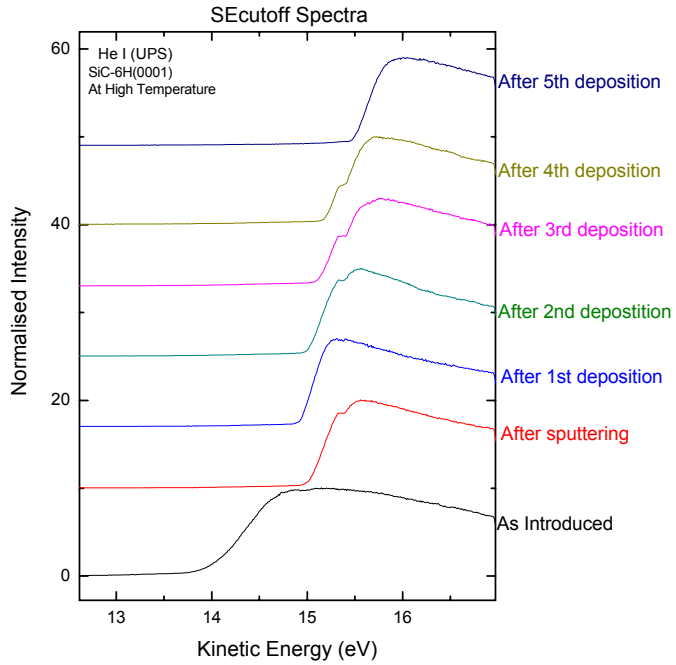


Figure 4-30 Secondary electron cut-off spectra of the third sample series.

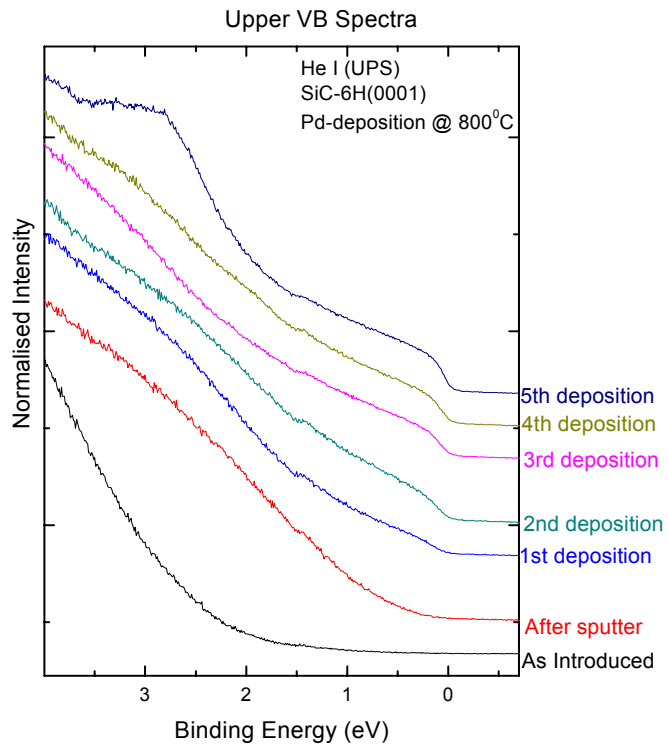


Figure 4-31 Upper valence band spectra of the third series.

From the spectra of the upper valence band, the valence band maximum can be determined as explained earlier. As the Pd deposition increases, the VBM shifts to lower binding energies, indicating that the sample is increasingly acquiring a metallic character at the surface.

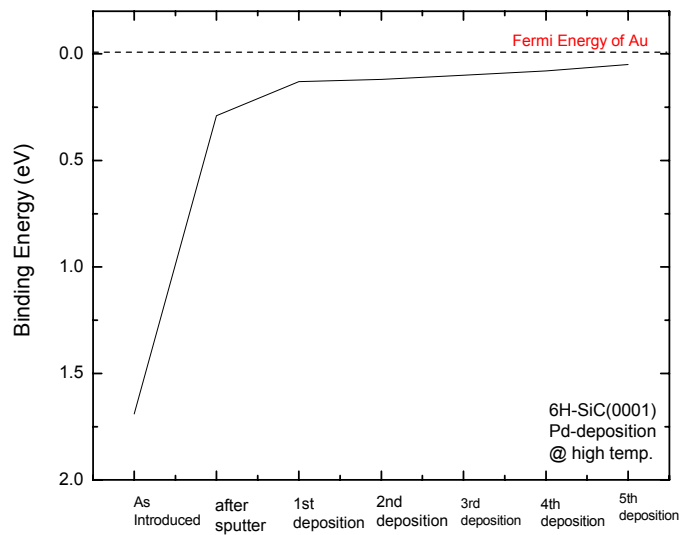


Figure 4-32 Position of the valence band maximum/Fermi edge for the third sample series.

The work function of the sample was measured and plotted in Figure 4-33. It increases gradually and hence indicating that the sample converts gradually to Pd metal.

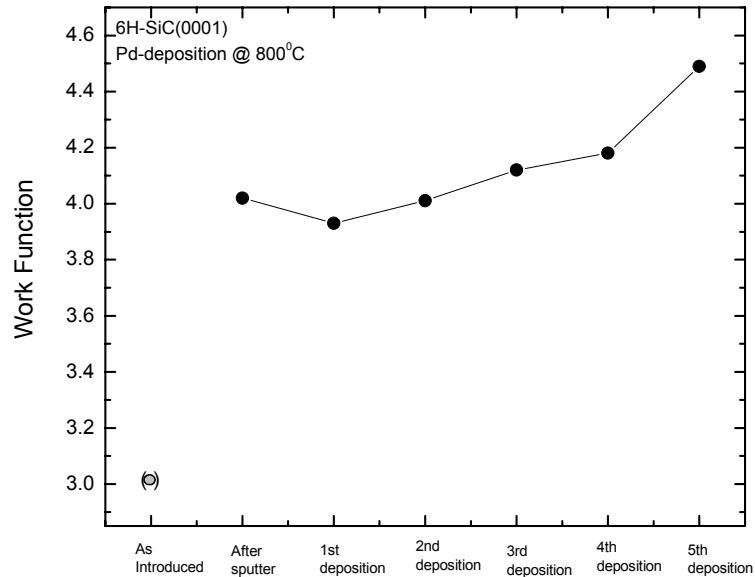


Figure 4-33 Work Function plot of the sample at each step.

4.4 Discussions

If a metal and semiconductor are brought into contact (as shown in Figure 4-34), generally a Schottky barrier is formed. The electrons start to flow from the semiconductor into the metal (if the work function of the metal is greater than that of semiconductor) until the Fermi energies of both solids are equal (equilibrium condition). In the semiconductor, a depletion region of width W is formed (uncompensated donors). In the metal, the electron transfer forms a negative surface charge layer. An electric field is created and hence an electric potential, which results in a band bending [38].

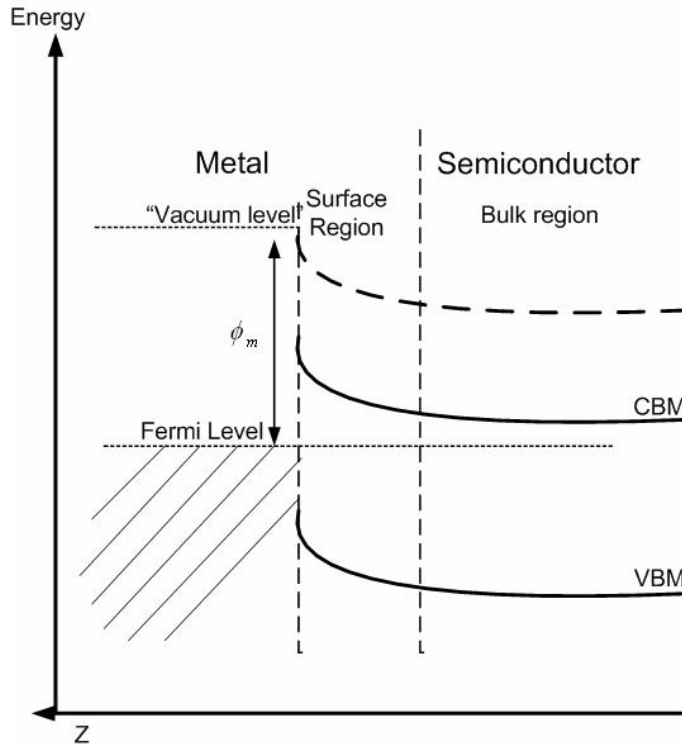


Figure 4-34 Formation of a Schottky barrier (for the case of metal with a larger work function than the semiconductor, as in the present case).

Note that the work function (Φ), i.e., the minimal energy required to remove an electron from the Fermi level to vacuum level, is a surface property and not defined for the bulk of a material (since no vacuum level is defined for the bulk). Nevertheless, most textbooks depict a vacuum level even within the bulk of the material, which is incorrect. In the diagrams of this thesis we have therefore included a hypothetical “bulk vacuum level”, depicted by a wide-dashed line. In contrast, the vacuum level at the surface, shown by the dotted line, is a well defined quantity. Since the work function is comprised of the chemical potential (μ) at the surface and the surface dipole (formed by a varying degree of the electron wave functions extending into the vacuum), it is strongly dependent on surface orientation and preparation. Furthermore, measurement is very

sensitive to sample misalignment and local fields in the vacuum chamber. In our case, we believe that, for example, the first data point in Fig. 4-33 is obscured by a misalignment problem. In all of our work function measurements, it is possible that the absolute values are too low, possibly due to a calibration problem. Nevertheless, differences between two measured work functions are reliable and accurate to within 0.2 eV or better.

In the experiments of series 2, the sample was first cleaned by sputtering cycles and then Pd was deposited layer by layer for five successive times. Figure 4-34 above shows the formation of metal/semiconductor junction with a *bulk* metal on the surface of a semiconductor where the work function of the metal is greater than that of the semiconductor. In the present case, the metal/semiconductor interface was gradually formed by stepwise deposition of Pd. As discussed above, the thinnest films don't even have a metallic character yet. We therefore have to augment the picture shown in Fig. 4-34 to a step-wise approach, as will be shown in the following.

4.4.1 Sample state after the sputtering cycles

As the SiC sample was cleaned by sputtering cycles and no Pd was yet deposited at this stage, the band structure of the sample is assumed to look as shown in Figure 4-35. Note that we are assuming flat-band conditions, which might not be the case in reality. For example, well-defined surface states or surface resonances can lead to significant charge accumulation at the surface, which induces a band bending. However, with surface sensitive techniques (as in our case), it is not possible to derive the band bending picture at the clean surface. We are hence assuming flat-band conditions, noting that the following discussion of band bending should be understood as a relative change with respect to the band positions on the sputter-cleaned surface.

In Figure 4-35, the measuring region on the sample, the work function of SiC (Φ_{SiC}), the regions measured by XPS and UPS, and the surface and bulk regions of the sample are shown.

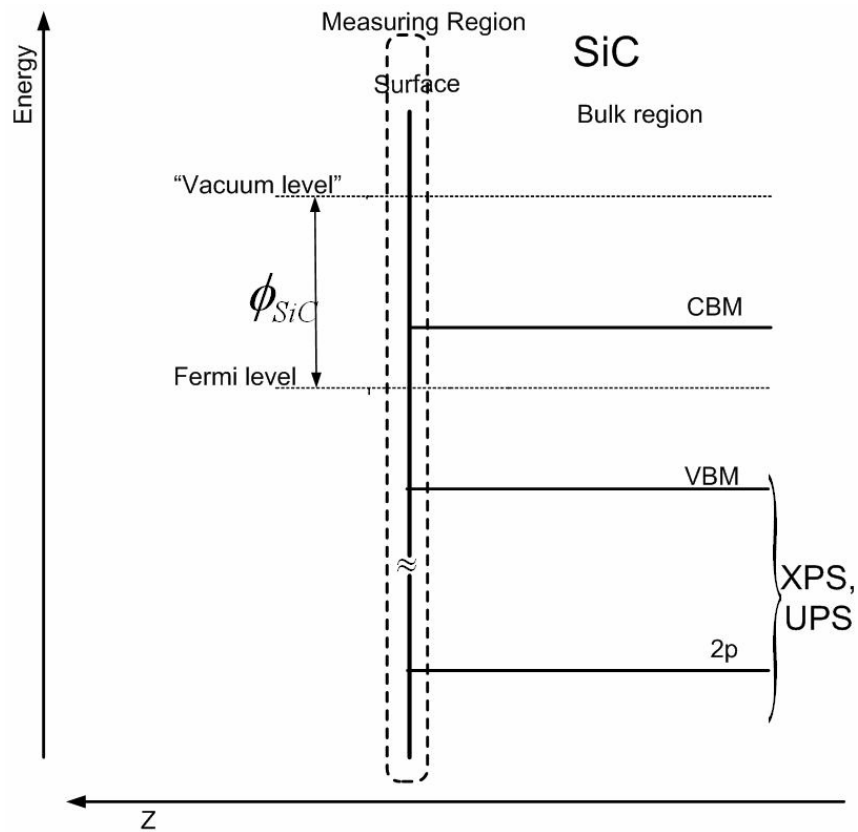


Figure 4-35 Band scheme of the sample after sputter-cleaning.

4.4.2 After the Pd deposition steps

After the first step, a very thin layer of Pd is formed on the SiC. The band scheme of the metal-semiconductor interface can be drawn as in Figure 4-36.

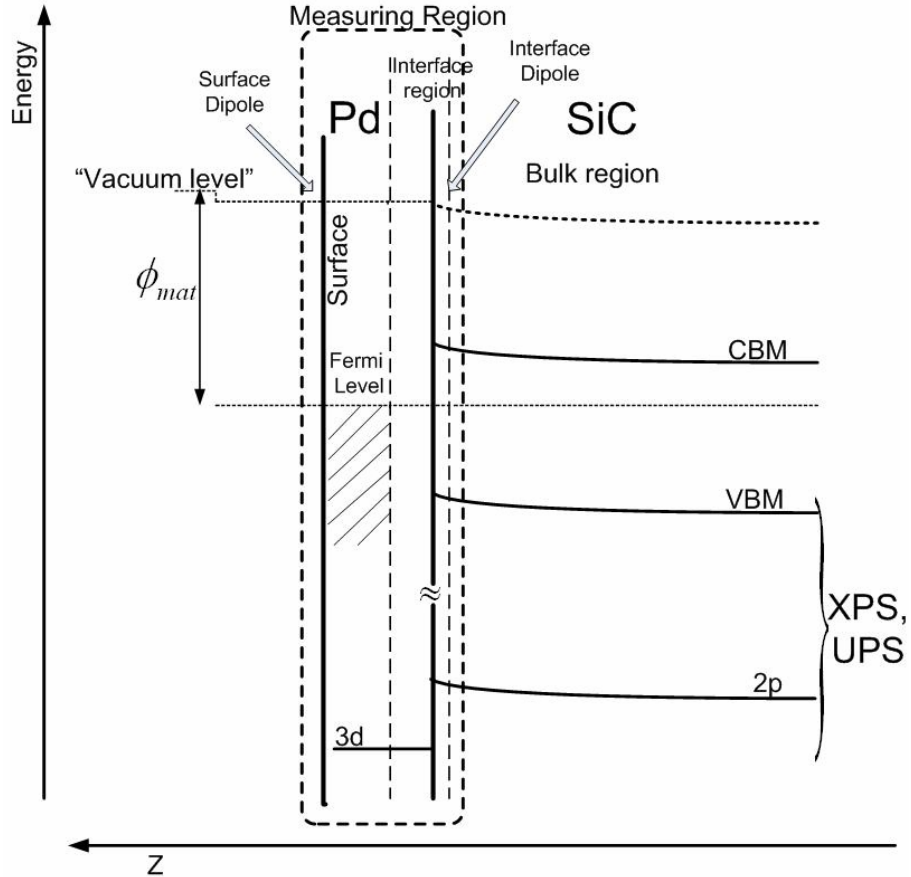


Figure 4-36 Band scheme of the Pd-SiC interface after the 1st Pd deposition.

Two different characteristic length scales need to be considered: on the scale of several atomic layers, the chemical bond is formed, presumably including some intermixing. This leads to a local and atom-specific shift of all electronic levels, as was discussed above. In the case of Pd/SiC, there is apparently a different chemical interaction for the room-temperature and the 800°C series, leading to a different shift for Si and C, respectively. This shift, induced by charge transfer on a short length scale, gives first indications on the chemical influence of Pd on SiC as a function of deposition temperature.

On the length scale of several hundred nanometers, electronic level alignment needs to be considered, as for any metal-semiconductor interface. Because the work function of SiC (4.8 eV) is less than that of Pd (5.1 eV), electrons will flow from SiC to Pd until the Fermi levels of both are aligned. Hence, a depletion region is formed at the surface of SiC. The negative charge accumulated at the metal and the uncompensated donors left at the surface of SiC build a potential at the interface, which leads to a band bending in SiC. Because, at first, only a very thin Pd layer is deposited, also the levels of the Pd shift when electrons flow from SiC to Pd in order to equalize the Fermi levels. Hence, the potential developed will be low and thus leads to a reduced bending of SiC bands. The work function (associated with the vacuum level), which, as mentioned above, is purely a property of the sample *surface*, increases, starting at the SiC work function and approaching the Pd work function with increasing coverage.

As the thickness of deposited Pd increases, the number of electrons that flow from SiC to Pd in order to align the Fermi levels increases which leads to an increase in band bending of the SiC bands, as shown in Figure 4-37. Once the Pd layer has reached a critical thickness, it will be sufficiently developed to supply the necessary screening charges for a fully-developed Schottky barrier. No further shifts of the bands are expected, even though there will still be some changes in the photoemission spectra, since the probing volume is increasingly moved into the Pd layer and away from the SiC “bulk”. Thus, for the thickest Pd layer on SiC in our experimental series, the band scheme of the sample will be similar to that of a bulk metal-semiconductor Schottky junction.

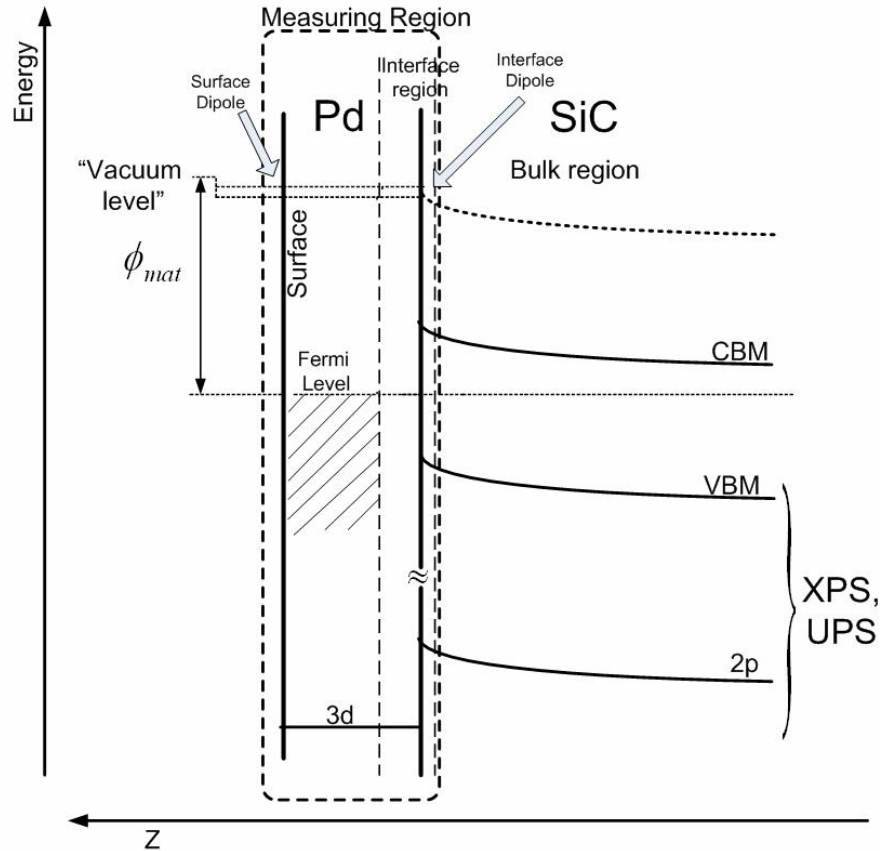


Figure 4-37 Band scheme of the Pd-SiC interface after further Pd deposition.

It is important to note that such band schemes are significantly complicated by the presence of dipoles, both at the surface (as discussed above) and the interface. In the latter case, short-range charge transfer can add to an overall electrostatic field at the interface, which would introduce a step in the hypothetical vacuum levels at the interface. Such interface dipoles can substantially influence the electronic behavior of junctions, and are indicative of a short-range mutual interaction of the junction partners. Finally, it is important to note that most (real-world) interfaces show some degree of intermixing, which might add to the complication of taking an interface dipole into account by “smearing out” this dipole across an extended range near the interface.

CHAPTER 5

CONCLUSIONS AND FUTURE WORK

5.1 Conclusions

In order to investigate the surface and interface properties of Pd/SiC and their chemical bonding behavior, which is the starting point to understand the diffusion and corrosion behavior of metal fission products (Pd) in TRISO coating materials, three experimental series were prepared. In the first series, a well ordered SiC(0001) surface was prepared and a monolayer of Pd was deposited onto the SiC single crystal at room temperature. The SiC substrate in series 2 was intentionally structurally disordered by extensive Ar-ion sputtering cycles with 2 keV ions to simulate the crystalline structure of TRISO SiC layers, which are not single-crystalline. The metal/semiconductor interface was formed at room temperature and the Pd layer thickness was successively increased. In order to study the impact of elevated temperatures, the SiC substrate in series 3 was not only structurally disordered (as in series 2), but the metal/semiconductor interface was also formed at higher temperatures (approx. at 800°C).

In series 1, two distinct carbon species on the SiC surface and three carbon species for the Pd/SiC interface were found. The two main species could be ascribed to a SiC bulk species and an interface species. In parallel, the Si 2p core levels also show the existence of two different Si species, both before and after the interface formation. In both cases,

there is an upward shift of all electronic levels, which indicates a change in surface band bending of the SiC substrate due to the formation of the metal/semiconductor interface.

In series 2, three chemical carbon species and two Si 2p species existed at the clean and uncovered SiC(0001) surface, which again can be ascribed to a bulk and an interface/surface species (a third species with low intensity was ascribed to adventitious carbon). The strong increase in intensity of the interface species during Pd deposition suggests an intermixing at the interface. There is a shift of all main peaks of the SiC substrate towards smaller binding energies, indicating a change in surface band bending of the SiC substrate due to the formation of the metal/semiconductor interface. Comparing the results of series 2 (room temperature) and 3 (800°C), we find significant differences in the local chemical environment of Si atoms upon the first Pd deposition step, indicating a different (temperature-dependent) reaction mechanism between Pd and SiC. For further steps, the evolution of the Pd/SiC interface, in particular in view of an upward band bending and the formation of a Schottky barrier, appears to be similar in both cases.

Thus, in summary, all the three experimental series shows an upward shift of all electronic levels indicating that there is band bending induced in the SiC substrate when Pd is deposited. Furthermore, there is significant charge transfer between Pd and SiC on various length scales. The interface species of all the species in all the experimental series is getting dominant as a function of Pd coverage, which is interpreted as a significant intermixing at the interface. Hence one can conclude that Pd interacts with SiC in several different ways, inducing local chemical bonding (corrosion), intermixing, and electronic structure modification. This, in turn, will impact the degradation of the SiC layer by Pd,

potentially leading to coating failure in TRISO nuclear fuel.

5.2 Future Work

For structural information, the samples described above are currently also being investigated with Transmission Electron Microscopy (TEM) for cross-sectional studies. Further analysis on Pd/SiC interface can be done by using X-ray Absorption Spectroscopy (XAS) and X-ray Emission Spectroscopy (XES). The results obtained should be tested by performing experiments on real TRISO SiC layers.

Based on the current experiments, it will be of large interest to conduct further experimental series by forming the Pd/SiC interface at even higher temperatures and by modifying the SiC surface prior to interface formation, e.g., by suitable plasma-etching procedures.

BIBLIOGRAPHY

- [1] R.L. Murray, Nuclear Energy, *Technology and Industrial Arts* (2000).
- [2] K. Minato, K. Fukuda, A. Ishikawa, N. Mita, Advanced coatings for HTGR fuel particles against corrosion of SiC layer, *J. Nucl. Mat.* 246 (1997) 215.
- [3] B.F. Myers, F.C. Montgomery, and K.E. Partain, *Doc No. 909055, GA Technologies Inc.*, (1986).
- [4] R.J. Lauf, T.B. Lindemer, and R.L. Pearson, Out-of-reactor Studies of Fission Product-Silicon Carbide Interactions in HTGR Particles, 172 (1990) 184.
- [5] Ronald L. Hockey, Pacific Northwest National Laboratory, Innovative Low-Cost Approaches to Automating QA/QC of Fuel Particle Production Using On-line Nondestructive Methods for Higher Reliability, *Proposal Number: 2002-103*
- [6] E. E. Morris and T. H. Bauer, Modeling of the Repository Behaviour of TRISO fuel, *ANL-AFCI-160 (2005)*.
- [7] K. Minato, T. Ogawa, K. Fukuda, K. Ikawa, and K. Iwamoto, Electron Probe Microanalysis of Irradiated Triso-Coated UO₂ Particles (II), *Japan Atomic Energy Research Institute*, Report JAERI-M 84-002 (1984).
- [8] T.N. Tieg, Fission-Product Pd-SiC interaction in Irradiated Coated-Particle Fuels, *Nucl. Technol.* 57 (1982) 389.
- [9] F. Montgomery, Fission Product-SiC Reaction in HTGR Fuel, General Atomic Company, Report DOE/ET/35300-T3 (1981).
- [10] K. Minato, T. Ogawa, K. Fukuda, S. Kashimura, M. Shimizu and Y. Tayama, Fission Product Palladium-Silicon Carbide Interaction in HTGR Fuel Particles, *J. Nucl. Mat.* 172 (1990) 184.
- [11] C. Heske, Interaction between metal fission products and TRISO coating materials: A study of chemical bonding and interdiffusion, Proposal for Task 17, Transmutation Research Program, UNLV.

- [12] L.I. Johansson, F. Owman, and P. Martensson, High-Resolution core-level study of 6H-SiC(0001), *Physical Review B* 53 (1996) 20.
- [13] L. Li and I.S.T. Tsong, *Surf. Sci.*, 351 (1996) 141.
- [14] F. Owman, and P. Martensson, *Surf. Sci.*, 369 (1996) 126.
- [15] Y. Hoshino, T. Nishimura, T. Yoneda, K. Ogawa, H. Namba and Y. Kido, Initial oxidation of 6H-SiC(0001)- $\sqrt{3}\times\sqrt{3}$ surface studied by ion scattering combined with photoemission induced by synchrotron-radiation-light, *Surface Science* 505 (2002) 234.
- [16] J. Bernhardt, M. Nerding, U. Starke and K. Heinz, Stable surface reconstructions on 6H-SiC(000 $\bar{1}$), *Materials Science and Engineering B* 61-62 (1999) 207.
- [17] A. Seubert, J. Bernhardt, M. Nerding, U. Starke, and K. Heinz, In situ surface phases and silicon-adatom geometry of the (2 \times 2)_c structure on 6H-SiC(000 $\bar{1}$), *Surface Science* 454-456 (2000) 45-48.
- [18] B. F. Rider, Compilation of Fission Product Yields, *General Electric Company*, GE Report NEDO-12154-3 (1981).
- [19] T. Namba, K. Minato, M. Yamawaki, and F. Fukuda, A Study on the Reaction between SiC and Pd, *Japan Atomic Energy Research Institute*, Report JAERI-M, 87-218 (1988).
- [20] H. Kleykamp, The Behavior of Fission Products in Highly Burnt HTR Fuels by Microprobe Analysis, Kernforschungszentrum Karlsruhe, Report KfK 2213 (1975).
- [21] R. Benz, R. Forthmann, H. Grubmeier, and A. Naoumidis, in: *Thermodynamics of Nuclear Materials* 1979, Vol. 1 (IAEA, Vienna, 1980) p. 565.
- [22] K. Minato, T. Ogawa, K. Fukuda, K. Ikawa, and K. Iwamoto, Electron Probe Microanalysis of Irradiated Triso-Coated UO₂ Particles (I), *Japan Atomic Energy Research Institute*, Report JAERI-M 83-200 (1983).
- [23] H. Kleykamp, *J. Nucl. Mater.* 131 (1985) 221.
- [24] K. Naito, T. Tsuji, T. Matsui, and A. Date, *J. Nucl. Mater.* 154 (1988) 3.
- [25] D. Petti, and J. Maki, The Challenges Associated with High Burnup and High Temperature for UO₂ TRISO-Coated Particle Fuel, *Idaho National Laboratory*, MIT NGNP Symposium.
- [26] C. L. Smith, SiC-Fission Product Reactions in Triso UC₂ and WAR UC_xO_y Fissile Fuel, Part I: Kinetics of Reactions in a Thermal Gradient, GA-A14313, *General Atomic Company* (Sep. 1977); also *J. Am. Ceram. Soc.* 62, 600 (1979).

- [27] R. L. Pearson, and T. B. Lindemer, The Interaction of LaC₂ and NdC₂ with SiC in HTGR Particles, Proc. Topl. Mtg. Thermal Reactor Safety, CONF-770708, Vol. 3, p.357, U.S. Department of Energy (1977).
- [28] Akio Kotani and Shik Shin, Resonant inelastic x-ray scattering spectra for electrons in solids, *Rev. of Modern Physics* 73 (2001) 203.
- [29] C.Heske, Spectroscopic investigation of buried interfaces and liquids with soft X-rays; *Appl. Phys. A* 78 (2004) 829-835.
- [30] S. Hüfner: Photoelectron Spectroscopy (Springer Ser. Solid-State Sci. 82) (Springer, Berlin, Heidelberg 1995).
- [31] D.Briggs and M.P.Seah, Practical Surface Analysis, second edition, volume 1, Chichester; New York: Wiley, 1983.
- [32] <http://www.uksaf.org/tech/xps.html>
- [33] R. L. Murray, Nuclear Energy: An Introduction to the Concepts, Systems, and Applications of Nuclear Process, Elsevier, fifth edition, 1920.
- [34] <http://www.mcallister.com/evappage.html>
- [35] A. Al-Hilfy, and R. Loudon, Effects of broadening mechanisms on atomic resonance fluorescence, *J. Phys. B: At. Mol. Phys.* 15 (1982) 2819.
- [36] F.P. Mc Cluskey, R. Grzybowski, and T. Podlesak, High Temperature Electronics, p101, 1996.
- [37] Nieuwenhuys, Bouwman, and Sachtler, *Thin Solid Films*, 21, 51, 1974.
- [38] A. Hiraki, Metal-Semiconductor Interfaces, first edition, Japan,1995, IOS press.
- [39] L. Lindell, P. de Jong, W. Ocikowicz, R. Lazzaroni, M. Berggren, W. R. Salaneck, X. Crispin, Characterization of the interface dipole at the paraphenylenediamine-nickel interface: A joint theoretical and experimental study, *J. of Chem. Phys.*, 122, 084712 (2005).

VITA
Graduate College
University of Nevada, Las Vegas

Goverdhan Reddy Gajjala

Local Address:

969 E Flamingo Rd
Apartment # 135
Las Vegas, Nevada 89119

Permanent Address:

Neelaiguda, Tripuraram mandal
Nalgonda Dt., Andhra Pradesh
India – 508207.

Degree:

Bachelor of Science, Electrical Engineering, 2003
Osmania University College of Engineering, India

Conferences:

Arizona-Nevada Academy of Science (ANAS) at UNLV, Feb. 2005

American Nuclear Society (ANS) Conference at Ohio State University,
Ohio, April 2005.

Thesis Title:

Interaction between Pd and SiC: a Study for TRISO Nuclear Fuel

Thesis Examination Committee:

Chairperson, Dr. Rama Venkat, Ph. D.
Graduate Faculty Representative, Dr. Clemens Heske, Ph. D.
Committee Member, Dr. Biswajit Das, Ph. D.
Committee Member, Dr. Sahjendra Singh, Ph. D.